

1 **Measurement Report: New particle formation characteristics** 2 **at an urban and a mountain station in Northern China**

3 Ying Zhou¹, Simo Hakala², Chao Yan^{1,2,*}, Yang Gao³, Xiaohong Yao³, Biwu Chu⁴, Tommy
4 Chan², Juha Kangasluoma^{1,2}, Shahzad Gani², Jenni Kontkanen², Pauli Paasonen², Yongchun
5 Liu¹, Tuukka Petäjä^{2,5}, Markku Kulmala^{1,2}, Lubna Dada^{2,6,7*}

6 ¹ Aerosol and Haze Laboratory, Beijing Advanced Innovation Center for Soft Matter Science and
7 Engineering, Beijing University of Chemical Technology, Beijing, China

8 ² Institute for Atmospheric and Earth System Research / Physics, Faculty of Science, University of
9 Helsinki, Finland

10 ³ Key Laboratory of Marine Environment and Ecology, Ministry of Education, Ocean University of
11 China, Qingdao 266100, China

12 ⁴ State Key Joint Laboratory of Environment Simulation and Pollution Control, Research Center for
13 Eco-Environmental Sciences, Chinese Academy of Sciences, Beijing 100085, China

14 ⁵ Joint International Research Laboratory of Atmospheric and Earth System Sciences (JirLATEST),
15 Nanjing University, Nanjing, China

16 ⁶ Extreme Environments Research Laboratory, Ecole Polytechnique Fédérale de Lausanne (EPFL)
17 Valais Wallis, Sion, 1951, Switzerland

18 ⁷ Laboratory of Atmospheric Chemistry, Paul Scherrer Institute, 5232 Villigen, Switzerland

19
20 **Correspondence to:* Lubna Dada: lubna.dada@helsinki.fi & Chao Yan: chao.yan@helsinki.fi

21 **Abstract**

22 Atmospheric new particle formation (NPF) events have attracted increasing attention for their
23 contribution to the global aerosol number budget, and therefore their effects on climate, air
24 quality, and human health. NPF events are regarded as a regional phenomenon, occurring
25 over a large area. Most observations on NPF events in Beijing and its vicinity were conducted
26 in populated areas, whereas observations on NPF events in mountain with few anthropogenic

emissions are still rare in Beijing (Wang et al. 2013). The spatial variation of NPF event intensity has not been investigated in detail by incorporating both urban area and mountain measurements in Beijing. Here, we provided NPF events characteristics in summer 2018 and 2019 at urban Beijing and a comparison of NPF event characteristics — NPF event frequency, particle formation rate, and growth rate — by comparing an urban Beijing site and a background mountain site separated by ~80 km from June 14 to July 14, 2019 as well as give insights into the connection between both locations. There were no significant difference of particle formation rates and growth rates observed during the short-term observation in 2019 and longer-term observation in summer 2018 and 2019 at the urban site. During parallel measurements at urban Beijing and mountain background areas, although the median condensation sink during the first two hours of the common NPF events was around 0.01 s^{-1} at both sites, there were notable differences in particle formation rates between the two locations (median of $5.42 \text{ cm}^{-3}\text{s}^{-1}$ at the urban site and $1.13 \text{ cm}^{-3}\text{s}^{-1}$ at the mountain site during the first two hours of common NPF events). In addition, the particle growth rates in the 7-15 nm range for common NPF events at urban site (median of $7.6 \text{ nm}\cdot\text{h}^{-1}$) at the urban site were slightly higher than those at mountain site (median of $6.5 \text{ nm}\cdot\text{h}^{-1}$). To understand whether the observed events were connected, we compared air mass trajectories as well as meteorological conditions at both stations. Favorable conditions for the occurrence of regional NPF events were largely affected by air mass transport. Overall, our results demonstrate a clear inhomogeneity of regional NPF within a distance of ~100 km possibly due to the discretely distributed emission sources.

Keywords: atmospheric aerosols, growth rates, regional new particle formation, sulfuric acid

1 Introduction

Atmospheric new particle formation (NPF) events resulting from the formation of clusters and stable aerosol particles from gas-phase precursors have been recognized as a major contributor to the global aerosol budget (Kulmala et al., 2004; Zhang et al., 2012). Once the newly formed particles grow to certain sizes, they can act as cloud condensation nuclei (CCN), affecting the regional and global climate (Pierce and Adams., 2009; Yu and Luo.,

55 2009). NPF events were also found to contribute to haze formation and thus can influence air
56 quality, especially in megacities where the precursor concentrations and associated particle
57 formation rates are rather high (Guo et al., 2014; 2020; Kulmala et al., 2021; Du & Dada et al.,
58 2021).

59 The occurrence of NPF events is a result of the competition between factors promoting and
60 inhibiting cluster formation and their growth. For instance, sufficient sulfuric acid and other
61 low-volatility vapors have been confirmed to be important in particle nucleation and growth
62 in field observations as well as in chamber experiments (Ehn et al., 2014; Wang et al.,
63 2017; Lehtipalo et al., 2018; Yao et al., 2018; Deng et al., 2020b). On the other hand,
64 background particles can inhibit new particle formation by acting as condensation sink for
65 vapor precursors and coagulation sink for newly formed particles. Indeed, Cai et al. (2017)
66 found that the Fuchs Surface Area (A_{Fuchs}) (which is linearly proportional to condensation
67 sink) determined the occurrence of NPF events in urban Beijing. In the atmosphere, ambient
68 conditions, such as air mass trajectories and meteorological conditions, can affect the
69 occurrence of NPF events by modifying the source-sink competition. Wu et al. (2007)
70 summarized favorable conditions for NPF events in Beijing based on a one-year observation
71 as sufficient solar radiation (sunny days), northerly wind, low relative humidity, and less
72 pre-loading large particles. Similarly, in other environments, plenty of radiation, intermediate
73 temperatures and low condensation sink favor the occurrence of NPF events (Qi et al.,
74 2015; Dada et al., 2017; Kerminen et al., 2018). Regional NPF events can happen with a
75 spatial extent up to several hundred kilometers and vertical extent from boundary layer to free
76 troposphere under favorable conditions (Hussein et al., 2009; Shen et al., 2011; Dai et al.,
77 2017). Earlier studies have shown that regional NPF events by simultaneous observations at
78 two or more sites had similar features in their occurrence and characteristics. For instance,
79 Komppula et al. (2006) investigated the occurrence of NPF events at two forest stations in
80 northern Finland during 2000-2003. Their results suggested that same air mass source regions,
81 favorable weather conditions and clean air at both stations were necessary for NPF events
82 occurring simultaneously at the two stations. Vana et al. (2016) compared observations at

83 three sites over 1000 km distance at northern Finland, southern Finland and Estonia in
84 2013-2014. They found that some events have the same origin. On the other hand, Jun et al.
85 (2014) observed that NPF events occurred less frequently at downtown Toronto than at a
86 nearby background site, and attributed this observation to the high condensation and
87 coagulation sink due to primary particle emission from traffic at urban areas. Moreover,
88 Carnerero et al. (2018) observed horizontal distribution and regional impact of the NPF
89 events with data from three urban, urban background, and suburban stations in the Madrid
90 metropolitan area, Spain in July 2016. Their results indicated that ultra-fine particles were
91 detected quasi-homogenously in an area spanning at least 17 km horizontally and the NPF
92 events extended over the full vertical extension of the mixed layer. Finally, Salma et al. (2016)
93 found that regional NPF events were modified and transformed by urban NPF events during
94 their observation in 2008-2009 and 2012-2013 in Budapest and at a regional background site
95 71 km away from it.

96 In comparison to the aforementioned studies in Europe, a similar study was also carried out to
97 understand the regional NPF events in North China Plain. Wang et al. (2013) characterized
98 the NPF events observed at an urban Beijing site and a regional background site about 120
99 km northeast to the urban site from March to November in 2008. They observed 96 and 87
100 NPF events at urban Beijing and background site, respectively, among which 52 NPF events
101 were observed simultaneously at both sites. They found that NPF events were slightly weaker
102 in the background site compared to those observed at the urban site. However, the factors that
103 influence the occurrence of NPF events at the two stations simultaneously were left
104 undetermined. In addition to largely populated urban areas, there is a large mountain area
105 within the Beijing-Tianjin-Hebei (BTH) region, where to our best knowledge, the
106 characteristics of NPF events are understudied. In this study, we conducted simultaneous
107 measurements of NPF event characteristics at an urban site in Beijing and a background
108 mountain site about 80 km west to urban Beijing from June 14 to July 14 2019.

109 Based on our observations, we aim to (i) compare the characteristics of the NPF events
110 between the two sites, including the frequency, particle formation rate, and particle growth

111 rate; (ii) figure out the connections and differences between NPF events at these two sites; (iii)
112 identify the favoring conditions for regional NPF events. Due to the profound participation of
113 NPF events in the global aerosol number loading and air quality degradation, identifying the
114 conditions that promote or inhibit the occurrence of regional scale NPF events could help
115 minimize its adverse effects.

116 **2 Experiment and methodology**

117 ***2.1 Sites' description***

118 Urban site: The Beijing University of Chemical Technology - BUCT (39.94° N, 116.31° E)
119 station is located on the fifth floor of a university building inside the west campus of BUCT.
120 The station is surrounded by several main roads with heavy traffic and residential areas and
121 thus, can be considered a typical urban station. More details of this station can be found in
122 Zhou et al. (2020). Observations at the urban site are continuous since January 17, 2018 and
123 were only interrupted for necessary instrument maintenance. The location is referred to as
124 'UB' from here after and is shown on the map in Fig. 1.

125 Mountain site: The Beijing Forest Ecosystem Research Station (39.96° N, 115.43° E) is
126 located in the west of Beijing, referred to as 'MT' from here after, which is part of the
127 Chinese Ecological Research Network (CERN). It is located in the mountain areas west of
128 Beijing, about 80 km from the urban site; see also in Fig. 1. The altitude of the station is 1170
129 m above sea level and it is surrounded by forests. The closest anthropogenic activities are
130 associated with small villages located in the valley nearby the MT station. Observations at
131 MT station are from June 14 to July 14, 2019. For comparison reasons, we only used the data
132 collected simultaneously at both stations.

133 ***2.2 Instrumentation***

134 Particle number size distribution data in the size range of 6-840 nm were collected using a
135 differential mobility particle sizer (DMPS) at the UB station. The instrument consists of one
136 Hauke-type DMA (differential mobility analyzer, home-built by university of Helsinki) in

137 different flow rates and one CPC (condensation particle counter, TSI Model 3772). Details of
138 this instrument can be found in Salma et al., 2011 and Kangasluoma et al. (2020). At MT
139 station, a scanning mobility particle sizer (SMPS, consists of a TSI Differential Mobility
140 Analyzer model 3081) and a fast mobility particle sizer (FMPS, TSI Model 3091) were used
141 to measure particle number size distribution from June 14 to June 28 and from June 29 to
142 July 14, respectively. The size ranges of the SMPS and FMPS are 7-1218 nm and 6.04-856
143 nm, respectively. The total number concentration from 4-3000 nm, measured by
144 Condensation Particle Counter (CPC; TSI Model 3775), was used to calibrate the particle
145 number size distributions from FMPS according to the method suggested by Zimmerman et
146 al. (2015). More details about the instrument are found in the previous studies (Wang et al.,
147 2019; Gao et al., 2020). The full campaign particle number size distributions at both sites are
148 shown in Fig. 2. The particle number size distribution measured by FMPS correlated well
149 with SMPS after being calibrated (Lee et al., 2013).

150 To ensure high quality of particle number size distribution data at UB site, a particle number
151 size distribution system (PSD) also sampled in parallel with DMPS from June 1 to August 31,
152 2019 (summer 2019). It included a nano-scanning mobility particle sizer (nano-SMPS, 3–55
153 nm, mobility diameter), a long SMPS (25–650 nm, mobility diameter) and an aerodynamic
154 particle sizer (APS, 0.55–10 μm , aerodynamic diameter). Details of this instrument can be
155 seen at Liu et al. (2016) and Deng et al. (2020b).

156 As shown in Fig.3, median particle number size distribution obtained from PSD and DMPS
157 matched well with each other within a factor of 2 during our observation in summer 2018 and
158 2019 at UB site. We cannot compare particle number size distribution data obtained from
159 DMPS, SMPS and FMPS as we did not sample with these three instruments in parallel at the
160 same site. However, it reasonable to assume that particle number size distribution obtained
161 from FMPS were comparable with those from DMPS as on one hand the measurement
162 techniques of particle number size distribution in the size range of these two instruments have
163 been well developed and be applied in quite a lot observations (Wang et al., 2017;
164 Kangasluoma et al., 2020), on the other hand, the FMPS was carefully calibrated and

165 properly operated during the observation as discussed above. Similar conclusions apply for
166 the SMPS as well where we can rely on using the measurement from this instrument to
167 discuss at least NPF event frequency at MT site during June 14 to June 28, 2019, during
168 which parameters of only one NPF event are calculated.

169 Sulfur dioxide (SO₂) concentration data were collected by Thermo Environmental Instrument
170 model 43i-TLE with a time resolution of 5-min at the UB station. There were no direct
171 measurement of SO₂ concentrations at the MT station, but the SO₂ measurement at the closest
172 national monitoring station (Longquan station, around 60 km from MT station and 20 km
173 from UB station, see Fig. 1) was used to indicate the strong decline of SO₂ concentration
174 from urban Beijing towards the west areas. Time series of SO₂ concentration at UB station
175 and Longquan station during the whole observation is shown in Fig. 4. Due to the lower
176 emission, the SO₂ concentration at the MT station is expected to be even lower than that in
177 Longquan station.

178 The sulfuric acid concentration was measured at UB station by a chemical
179 ionization-atmospheric interface-time of flight mass spectrometers (CI-APi-ToF, Aerodyne
180 Research Inc.) equipped with a nitrate chemical ionization at UB station (Lu et al.,
181 2019). There were no sulfuric acid data available at MT station and since no SO₂
182 concentrations were available, a sulfuric acid proxy concentration could not be derived.

183 The meteorological conditions such as relative humidity (RH, %), temperature (°C) and solar
184 radiation (UVA and UVB, W/m²) were measured using a Vaisala Weather station data
185 acquisition system (AWS310, PWD22, CL51), Metcon at UB station and using Vaisala
186 MAWS301 automatic weather station at MT station. The measurements at the MT station
187 were carried out at the height of 1.5 m. The wind speed (m/s) and wind direction (°) data is
188 also measured by the weather station at UB site, while at MT site, we obtained with
189 reanalyzed data from ERA5 model (Olauson, 2018).

190 *2.3 Air mass back trajectories*

191 Air mass back trajectories were calculated using a Lagrangian particle dispersion model

192 FLEXPART (FLEXible PARTicle dispersion model) version 9.02 (Stohl et al., 2005). As the
193 meteorological input, we used ECMWF (European Centre for Medium-Range Weather
194 Forecast) operational forecast data with 0.15° horizontal and 1-hour temporal resolution.
195 Particle retroplume simulations were performed hourly for both sites during the whole study
196 period. For each retroplume simulation, we used 50 000 model particles distributed evenly
197 between 0–100 m above the measurement site. The released model particles were traced
198 backwards in time for 72 h, unless they exceeded the model grid ($20\text{--}60^\circ\text{N}$, $95\text{--}135^\circ\text{E}$,
199 resolution: 0.05°).

200 Based on the arrival direction of the 72-h backward trajectories, the prevailing air mass
201 transport conditions at each site were classified into 5 groups: North group, West group, East
202 group, South group and Local group. Air masses arriving from north, north-west and
203 north-east including Mongolia, Inner-Mongolia and north-east China were classified into the
204 North group. Air masses from Shanxi province, Inner-Mongolia and further west were
205 classified into the West group. Air masses from the ocean east of Beijing were classified into
206 the East group and air masses from southern areas were classified into the South group.
207 Stagnant air masses that had only travelled short distances and/or were circulating around the
208 measurement site were classified into the Local group. Examples of air mass trajectories
209 belonging to these five groups are shown in Fig. 5. In general, air masses from the north and
210 west supply clean air from the mountainous areas to both stations, whereas air masses from
211 the east and south travel over highly populated areas, thus accumulating air pollutants.
212 However, the impact of local air masses on the pollution levels at the two sites can be
213 different; at UB station, local air masses are polluted by the urban emissions, while at MT
214 station stagnant air could cause a clean situation due to low local emissions. More details on
215 the relationship between air mass transport conditions and the extent of pollution is discussed
216 in later sections.

217 *2.4 Estimating the spatial extent of NPF*

218 The observation of regional new particle formation events, where the growth of newly
219 formed particles can be followed for several hours, is a result of NPF taking place over a

220 large spatial area. This is because as time progresses, the particles observed at a measurement
221 site must have originated from further and further away due to non-zero wind conditions.
222 Following the progression of the observed NPF event and using air mass back trajectories, we
223 can estimate where the particles observed at different stages of the NPF event were initially
224 formed by calculating the air mass locations at the onset time of the NPF event (assuming
225 that NPF occurs simultaneously over the larger area). Typically, the mode related to the NPF
226 event disappears from the observations after some time. This is an indication of the currently
227 observed air mass arriving from an area where NPF was no longer taking place due to
228 unfavorable local conditions. If the shift in the air mass origin towards unfavorable conditions
229 occurs gradually over time, the mode related to the NPF event can enter a stage of growth
230 stagnation (or even decrease in size) before disappearing completely (Kivekäs et al., 2016).
231 This is because the increasing transport time between NPF onset and observation of the
232 particles at the measurement site provides less and less additional ‘material’ for aerosol
233 growth towards the more unfavorable conditions. Calculating the locations where NPF is
234 assumed to have taken place for longer data sets including several regional NPF events can
235 give an estimation of the typical spatial extent of NPF around the measurement location. It
236 should be noted that even in relatively clear cases, the subjective determination of NPF event
237 onset and end times can easily lead to uncertainties of few tens of kilometers in the
238 estimations. In locations with strong primary pollution sources, such as urban Beijing,
239 objective determination of said times becomes even more difficult. More details and
240 discussion related to the method and its uncertainties can be found in Kristensson et al.
241 (2014).

242 ***2.4 NPF event classification***

243 Particle number size distribution data from both stations were used for classifying individual
244 days into new particle formation (NPF) event days and non-event days. This classification
245 followed procedures presented by Dal Maso et al. (2005) and later adapted for urban
246 locations (Chu et al., 2021) in which a day is classified as a NPF event day if (a) a new mode

247 in the size range smaller than 25 nm appeared and (b) the new mode kept growing over
248 several hours. On the other hand, non-event days are the days which do not fit any of the
249 abovementioned criteria and undefined days are the days which fit either one of the
250 abovementioned criteria or the days which we cannot distinguish whether the new mode was
251 from NPF event or traffic.

252 **2.5 Characteristics of NPF events**

253 *2.5.1 Condensation sink*

254 The condensation sink (CS) was calculated from particle size distribution data using the
255 method described by Kulmala et al. (2012):

$$256 \quad CS = 2\pi D \sum_{dp'} \beta_{m,dp'} dp' N_{dp'}$$

257 (1)

258 where D is the diffusion coefficient of the condensing vapor, sulfuric acid in our case, and
259 $\beta_{m,dp'}$ represents the transition-regime correction, $N_{dp'}$ is the particle number concentration
260 with diameter dp' . As shown in Fig. 6, particles in size range of 20-800 nm dominated the
261 total CS at UB station and particles in the size range of 50-800 nm dominated the total CS at
262 MT station. Although the size ranges of DMPS, FMPS and SMPS slightly differ, all of them
263 cover the main size range which constituted the CS and thus the calculation of CS should not
264 be significantly influenced by differences in the instrument size ranges.

265 *2.5.2 Particle growth rates*

266 Particle growth rates were calculated for the size range of 7-15 nm ($GR_{7-15 \text{ nm}}$) using the 50%
267 appearance time method introduced by Lehtipalo et al. (2014) and Dada et al. (2020a)
268 according to

$$269 \quad GR = \frac{dp_2 - dp_1}{t_2 - t_1}$$

270 (2)

271 where t_2 and t_1 are the appearance times of particles with sizes of dp_2 and dp_1 , respectively.
 272 The appearance time is defined as the time at which the concentration of particles at size d_p
 273 reaches 50% of its maximum.

274 2.5.3 Particle formation rates

275 The formation rates of particles of diameters 7 nm (J_7) were calculated from particle number
 276 size distribution data using the method presented by Kulmala et al. (2012) and modified for
 277 urban environments by Cai and Jiang (2017):

$$J_k = \frac{dN_{[d_k, d_u]}}{dt} + \sum_{d_g=d_k}^{d_u-1} \sum_{d_i=d_{min}}^{+\infty} \beta_{(i,g)} N_{[d_i, d_{i+1})} - \frac{1}{2} \sum_{d_g=d_{min}}^{d_u-1} \sum_{d_i^3=\max(d_{min}^3, d_k^3-d_{min}^3)}^{d_{i+1}^3+d_{g+1}^3 \leq d_u^3} \beta_{(i,g)} N_{[d_i, d_{i+1})} N_{[d_g, d_{g+1})}$$

$$+ \left. \frac{dN}{dd_i} \right|_{d_i=d_u} \bullet GR_u$$

278

279 (3)

280 Here, J_k is the particle formation rate at size d_k , $\text{cm}^3 \cdot \text{s}^{-1}$, (7 nm in this study); d_u is the upper
 281 size limit of the targeted aerosol population (10 nm in this study); d_{min} is the smallest particle
 282 size detected by particle size spectrometers (to make the results comparable, the d_{min} was set
 283 to 7 nm); $N_{[d_k, d_u]}$ is the number concentration of particles from size d_k to d_u ; d_i represents the
 284 lower limit of the i^{th} size bin; $\beta_{(i,g)}$ is the coagulation coefficient for the collision of two
 285 particles with the size of d_i and d_g ; and GR_u refers to the particle growth rate at size d_u , $\text{nm} \cdot \text{h}^{-1}$
 286 Deng et al. (2020b).

287 3 Results and discussion

288 3.1 NPF event frequencies at both stations

289 During our observation in summer 2018 and 2019 (from June to August of each year) at UB
290 station, there were 155 days with valid data, 53 days of which were classified as NPF event
291 days, corresponding to an NPF event frequency of 34%. This NPF event frequency was
292 consistent with observations in urban Beijing in 2004 and 2008 in summer while smaller than
293 other seasons especially winter during those observations and the observation in UB station
294 (Wu et al., 2007; Wang et al., 2013; Deng et al., 2020b).

295 For comparison of NPF characters between UB and MT stations, a parallel short-term
296 observation was conducted at MT station from June 15 to July 14, 2019. In Fig.2, we show
297 the particle number size distribution and CS during our short-term observations at both
298 stations. There were a total of 12 and 13 NPF events observed at the UB station and the MT
299 station, corresponding to an NPF event frequency of 48% (12 of 25) and 52% (13 of 25),
300 respectively. Only days when particle number size distribution data were valid that visual
301 inspection of the data and the number concentrations as well as instrument status do not
302 indicate problems in the measurements for both stations were taken into consideration in our
303 analysis. In addition, 9 NPF events were observed at both stations on the same day (referred
304 to as common NPF events). Detailed information on the classified NPF event and non-event
305 days, including the particle formation rates, growth rates, as well as their associated air mass
306 origins during the short-term observation are provided in Table 1.

307 In order to understand the conditions favoring NPF events at both stations, we analyzed
308 various ambient parameters including air mass trajectories, meteorological variables,
309 condensation sink as well as sulfuric acid concentration.

310 3.1.1 Favorable air mass origin for NPF events at individual locations

311 In Fig.7, we show frequencies of air masses arriving at UB station from different directions
312 during our observation in summer 2018 and 2019. The most frequent air masses arriving at
313 UB station belonged to the South group. During our observation in the two summers, out of

314 155 days were 52 days belonging to the South group and 39, 32, 9 and 23 days in air masses
315 belong to North, East, West and Local groups, respectively. NPF event frequency with respect
316 to air masses is also shown in Fig. 7. It is noticeable that air mass origin influenced the
317 occurrence of NPF events at UB site as the majority of NPF events occurred when the air
318 masses were coming from the north. During our observation in summer 2018 and 2019, 34
319 (out of 55) NPF events occurred in air masses from the North group and 9, 2, 2 and 6 NPF
320 events in the South, East, West and Local groups, respectively (Fig.7a). One prominent
321 feature of these air masses is their difference in CS. The CS of the air masses classified as the
322 North group (with median values of 0.01 s^{-1} at UB station) is substantially lower than that in
323 other air mass classes (CS = 0.03, 0.025, 0.017, 0.03 s^{-1} , for south, east, west and local,
324 respectively), which might explain the high NPF event frequency associated with this air
325 mass class. During the observation from June 14 to July 14 in summer 2019, the most
326 frequent air masses arriving at both sites belonged to the North group as shown in Table 1.
327 Out of 25 days, there were 8 and 9 days belonging to the North group, at UB and MT sites,
328 respectively. The highest frequency of NPF events also occurred when the air masses were
329 coming from the north. The high NPF events frequency during our observation from June 14
330 to July 14 could also be attributed to the frequent air masses arriving at both sites from north
331 to Beijing.

332 As shown in Table 1, NPF events occurring simultaneously at both sites only happened when
333 air masses arrived at both sites from the same directions, suggesting that most of the observed
334 NPF events took place over the whole studied area, extending for several hundreds of
335 kilometers (Dai et al., 2017; Du et al., 2021). The occurrences of common NPF events also
336 closely connected with air mass origins that 7 (out of 9) common NPF events occurred under
337 air masses in the North group, with the other two NPF events in the South group.

338 *3.1.2 The role of condensation sink in NPF event occurrence*

339 Figure 8a shows the difference in CS between NPF event and non-event days during our
340 observation in summer 2018 and 2019 (two whole summers) at UB site and short-term
341 parallel observations at both sites. The ‘NPF1’ and ‘non-event1’ referred to NPF and

342 non-event days during the two whole summers, respectively, while ‘NPF2’ and ‘non-event2’
343 referred to NPF and non-event days during the short-term parallel observation period from
344 June 14 to July 14, 2019 at both sites, respectively. The longer-term periods are used for
345 confirming the representativeness of the short-term overlapping period for the whole summer.
346 As shown in the figure, the median CS on NPF1 or NPF2 days is equivalent for UB station
347 ($CS_{NPF1} = 0.010s^{-1}$; $CS_{NPF2} = 0.009s^{-1}$) and less than a factor of 1.2 different between
348 non-event1 and non-event2 in UB station ($CS_{nonevent1} = 0.023s^{-1}$; $CS_{nonevent2} = 0.020s^{-1}$), which
349 confirms the representativeness of our short-term measurement period to the overall urban
350 Beijing summer.

351 Our results in figure 8a show that the median CS was $\sim 0.01 s^{-1}$ during the first 2 hours of the
352 NPF events, at both stations. On common NPF event days, the median CS was $0.009 s^{-1}$ at
353 UB station and $\sim 0.01s^{-1}$ at MT station, respectively. In comparison, on non-event days,
354 during roughly the same time period (9:00–11:00 LT), the CS was substantially higher, with
355 median values of $0.02 s^{-1}$ and $0.014 s^{-1}$, at UB and MT stations, respectively. Figure 8b
356 presents the median CS during the first 2 hours of NPF events on common NPF event days
357 measured at both stations, and shows the high correlation between the two.

358 Figure 8c shows the NPF event frequency as a function of CS during our observation at UB
359 site in summer 2018 and 2019 and how the NPF event frequency decreased with increasing
360 CS. When CS was smaller than $0.01 s^{-1}$, all days were classified as NPF event days, and when
361 CS was larger than $0.035 s^{-1}$, no day was classified as NPF event day. This shows the major
362 role of background particles in controlling the occurrence or inhibition of NPF events as
363 shown in several previous studies in China and internationally (Deng et al., 2020a; Cai et al.,
364 2017; Kulmala et al., 2017). While we cannot present a similar figure from the MT station,
365 the same conclusion applies where CS does play a role in inhibiting NPF observation owing
366 to the difference in the CS values observed between NPF and nonevents at MT as shown in
367 figure 8a. Yet, since the overall preexisting particle concentration at the MT is rather on the
368 low end, the role of CS might not be as vital at the MT station as for the UB station.

369 Different from NPF events under low CS ($<0.01 s^{-1}$), these NPF events under high CS were

370 characterized by a relatively high H_2SO_4 concentration ($>10^7 \text{ cm}^{-3}$) or low particle formation
371 rates (Fig.9a), discussed in further details in the coming sections. In comparison, at MT
372 station, when CS was smaller than $\sim 0.013 \text{ s}^{-1}$, most (10 out of 14) days were classified as
373 NPF event days as shown in Fig. 9d. When CS was larger than $\sim 0.013 \text{ s}^{-1}$, we only observed
374 one local NPF event and another two non-local NPF events (Table 1). The local NPF event
375 under high CS at the MT station was characterized as high UV ($>30 \text{ W/m}^2$) and low
376 formation rate (J_7 were too small to be reliably calculated) as well.

377 *3.1.3 Role of meteorological variables in NPF event occurrence*

378 While the air mass source regions, and their connection to the CS, seem to explain the general
379 picture of NPF event occurrences at the two sites well, we still have some cases unexplained.
380 For example, as shown in Table 1, there were several non-event days observed at MT station
381 with air masses belonging to North and West groups, which were connected to low CS. This
382 indicates that a further investigation into other NPF-related variables is still required.

383 In Figure 10, we show diurnal variation of meteorological variables during our observation in
384 summer 2018 and 2019 at UB site and observations from June 14 to July 14 in 2019 at UB
385 and MT sites. It is noticeable that the short-term observation compared well with the
386 long-term observation and therefore is representative of summer at UB site as shown in
387 Fig.10.

388 First, the intensity of solar radiation is considered one of the most important parameters
389 deciding NPF event occurrence as it translates into photochemistry strength (Chu et al., 2019).
390 The median UV (UVA+UVB) intensity at the UB station on NPF event and non-event days
391 was 38.3 and 32.9 W/m^2 , respectively. The UV intensity was on average $\sim 15\%$ higher on
392 NPF event days than on non-event days at UB station. Although UV intensity was important
393 for NPF event occurrence, we still observed NPF events at UB station under low UV intensity,
394 e.g. cases on June 30 and July 6. These two events all started immediately after sunrise (6:30
395 LT on June 30 and 7:00 LT on July 6, see Table 1) and median UV intensity during the first
396 two hours of NPF events was only 13.2 and 14.1 W/m^2 , respectively. However, sulfuric acid
397 concentration was higher than 10^7 cm^{-3} at the same time, the possible reason is high SO_2

398 concentration and low CS ($\sim 0.003 \text{ s}^{-1}$) outcompeted the low UV intensity (Dada et al., 2020b)
399 as well as the possibility of having other H_2SO_4 sources (Yao et al., 2020).

400 At MT station, the median UV intensity on NPF event and non-event days was 28.4 and 14.2
401 W/m^2 , respectively. The lower UV at MT station, in general might be related to the higher
402 RH (Fig. 10c&d) and thus more cloudiness and fog at the MT station (Hamed et al.,
403 2010; Dada et al., 2018). The UV intensity was on average $\sim 100\%$ higher on NPF event days
404 than on non-event days at UB station. All local NPF events happened when UV intensity was
405 higher than 15 W/m^2 as shown in Fig. 9d.

406 On the other hand, as shown in Fig. 10c&d, the median relative humidity (RH) was lower on
407 NPF event days than non-event days at both stations. This is consistent with earlier results
408 that high RH suppressed NPF events by increasing CS and coagulation sink (CoagS), as it
409 can enhance the particle hygroscopic growth (Hamed et al., 2010; Hamed et al., 2011). In
410 addition, high RH was also found to be associated with more clouds resulting in less solar
411 radiation (Dada et al., 2018).

412 The median temperatures at UB on event and non-event days were $31 \text{ }^\circ\text{C}$ and $29 \text{ }^\circ\text{C}$,
413 respectively, and at MT station $23 \text{ }^\circ\text{C}$ and $19 \text{ }^\circ\text{C}$, respectively. The median temperature was
414 lower at the MT station than at the UB station, due to the higher altitude of the station and
415 likely also the weaker solar radiation (Fig. 10e&f). At both stations, the median temperature
416 was very similar on NPF event and non-event days, suggesting that temperature was not a
417 crucial factor for NPF event occurrence during the measurement in summer.

418 *3.1.4 Role of sulfuric acid concentrations in NPF event occurrence*

419 Sulfuric acid has been found to be the main precursor vapor participating in NPF in China
420 and in many locations around the world due to its low volatility (Yao et al., 2018; Chu et al.,
421 2019). In Fig. 9a, we show the concentration of sulfuric acid as a function of CS during
422 summer 2018 and 2019 at UB site. As shown in Fig. 9b, the median sulfuric acid (H_2SO_4)
423 concentrations at UB station were $8.1 \times 10^6 \text{ cm}^{-3}$ and $4.5 \times 10^6 \text{ cm}^{-3}$ on NPF event days and
424 non-event days, respectively, during observation from June 14 to July 14 in 2019 and 7.9×10^6
425 cm^{-3} and $3.4 \times 10^6 \text{ cm}^{-3}$ on NPF event days and non-event days, respectively, during the

426 observation in summer 2018 and 2019. This suggests that H_2SO_4 was important for NPF
427 events at the UB station (Deng et al., 2020b; Dada et al., 2020b). On the other hand, as shown
428 in Fig.9a, the H_2SO_4 concentration during 9:00- 11:00 (local time) on non-event days could
429 be comparable with that on NPF event days, especially when CS was high. The H_2SO_4
430 concentration during 9:00- 11:00 (local time) on non-event days could be comparable with
431 that on NPF event days, especially when CS was high. Altogether, our observation shows that
432 the occurrence of NPF events was controlled by both H_2SO_4 and CS at the UB station (Cai et
433 al., 2020).

434 In addition, although we did not perform the measurement of H_2SO_4 at the MT station,
435 concentration of H_2SO_4 is expected to be much lower than that at the UB station. First, the
436 SO_2 concentration at measurement at Longquan Town was always below the detection limit
437 (~ 0.5 ppb) during our observation period. In comparison, median SO_2 concentration at UB
438 station was 0.87 ppb for all days and 0.65 ppb for NPF event days during our short-term
439 parallel observation period. The spatial decreasing trend of SO_2 concentration from urban
440 Beijing to the west implies a low SO_2 concentration at the MT station, especially when the
441 nearby anthropogenic sources are sparse (Liu, 2008; Ying, 2010; Wang, 2011; Yang-Chun et al.,
442 2013). Second, the oxidation of SO_2 by photochemistry reactions could also be limited by the
443 low solar radiation at the MT station as we discussed in 3.1.3. Third, CS, as the main sink of
444 H_2SO_4 , was comparable at the MT station to that in the UB station on NPF event days (as
445 shown in Fig.8a). Altogether, the lower production rate and the equivalent loss rate of H_2SO_4
446 at the MT station likely results in the lower H_2SO_4 concentration, in comparison to UB
447 station.

448 Due to the lack of H_2SO_4 measurement, the NPF mechanism at the MT station cannot be
449 inferred. Nevertheless, we show that the occurrence of NPF as a response to photochemistry
450 (and very likely to H_2SO_4) and CS in Fig. 9d. It is clear that high UV intensity and low CS
451 favored the occurrence of NPF. However, there existed exceptions. For example, two NPF
452 events were observed even when the UV intensity was low and the CS was high, besides, it
453 was an undefined day on June 28 despite of the high UV intensity and low CS. These

454 exceptional cases will be discussed in detail in Section 3.6.1 and 3.6.2, respectively.

455 **3.2 NPF event start time at both stations**

456 There was no significant difference in NPF event start time between the long-term and
457 short-term parallel observations at UB site. In this section, we only compare NPF event start
458 time of common events at UB and MT sites during the short-term parallel observations.

459 During our observation, there was no advection of air masses between the two sites on
460 common NPF event days, indicating that the NPF events occurred at each site independently.

461 As shown in Table 1, all common NPF events started after sunrise and prior to noon except
462 the two non-local NPF events at MT station. However, NPF event start time was different
463 between the two sites. Earlier researches in Nanjing, China and Nordic stations showed the
464 similar results that NPF events can be observed simultaneously at two or more sites, but the
465 start time can be different, local meteorology, source strength and background aerosols could
466 drive temporal behavior of NPF events at each sites (Hussein et al., 2009; Dai et al., 2017).

467 **3.3 Particle formation and growth rates at both stations**

468 The particle formation rates (J_7) at the two stations during the measurements are presented in
469 Fig.11a. J_7 observed during the short-term parallel observation (NPF2) at UB site was in the
470 range of 3.0-10.0 $\text{cm}^{-3} \text{s}^{-1}$ with a median of 5.4 $\text{cm}^{-3} \text{s}^{-1}$, comparable with those observed in
471 summer 2018 and 2019 (NPF1 = 2-14.0 $\text{cm}^{-3} \text{s}^{-1}$ with a median of 4.9 $\text{cm}^{-3} \text{s}^{-1}$) and
472 significantly higher than the values in the MT station (0.75-3.0 $\text{cm}^{-3} \text{s}^{-1}$ with a median of 0.82
473 $\text{cm}^{-3} \text{s}^{-1}$) for common NPF events (Fig.11b). These values are comparable to earlier
474 observations in urban Beijing and another regional background station in North China Plain
475 (NCP) (Wang et al., 2013). Earlier observations in NCP and Yangtze River Plain also
476 observed higher formation rates at urban sites than corresponding background sites by
477 roughly a factor of 2 due to lower anthropogenic emissions at background sites (Wang et al.,
478 2013; Dai et al., 2017; Shen et al., 2018). The much lower J_7 observed at MT station is very
479 likely associated with the low H_2SO_4 concentration at this station, as we discussed above.

480 However, other reasons, such as the low concentration of H₂SO₄ stabilizers, e.g., amines,
481 cannot be ruled out either. Also, the J_7 at UB station could be affected by particle emissions
482 due to the proximity of the location to the highway (Kontkanen et al., 2020).

483 The particle growth rates in size range of 7-15 nm (GR_{7-15nm}) at the UB station (4.8-12.9
484 nm/h with a median of 7.8 nm/h) during NPF2 was also comparable with the whole summers
485 (NPF1) (4.8-12.9 nm/h with a median of 8.5 nm/h). While the difference in J_7 was 7 times
486 higher in UB than in MT, the observed GR were only a slightly higher at UB than at the MT
487 station (5.7-10.5 nm/h with a median of 6.5 nm/h) for common NPF events (Fig.11c&d),
488 implying that precursors needed for particle formation were much more abundant in the
489 polluted urban environment (Wang et al., 2013), while those needed for growth are rather
490 comparable. The GR at UB station was comparable with other long-term observation at UB
491 station (1.1-8.0 nm/h) in 2018, and other urban areas in China (Herrmann et al., 2014; Chu et
492 al., 2019; Deng et al., 2020b). Consistent with earlier observations showing that H₂SO₄ could
493 only contribute to a small fraction of the particle growth at this size range (Paasonen et al.,
494 2018; Qi et al., 2018; Guo et al., 2020), the growth rates at both stations cannot be explained
495 by the H₂SO₄ concentration. This implies that other condensable species, very likely
496 low-volatility organic vapors, play an important role in particle growth at both stations. At the
497 UB station, anthropogenic VOCs are dominant precursors of these low-volatility organic
498 vapors (Guo et al., 2020; Deng et al., 2020a), while VOCs at MT station, with rare
499 anthropogenic sources, are likely dominated by biogenic emissions.

500 ***3.4 Ending diameters of newly-formed grown particles***

501 Earlier observations have shown that diameters of newly-formed particles should be larger
502 than 70 nm to contribute to cloud condensation nuclei significantly (Man et al., 2015; Ma et
503 al., 2021) and will be considered as haze particles when their size reaches larger than 100 nm
504 (Kulmala et al., 2021). In Fig. 12, we show ending diameters (End D_p) of newly formed
505 grown particles during our observations at both sites. End D_p during the observation from
506 June 14 to July 14 at UB site (21-105 nm, with a median of 49 nm, Fig.12a) had similar

507 characteristics as those during the long-term observation in summer (21-126 nm, with a
508 median of 56 nm, Fig.12a) where most of End Dp were in the range of 25-70 nm. As shown
509 in Fig.12b, 61% of End Dp were in the range of 25-70 nm, and only 9% of End Dp were
510 larger than 100 nm during our observation in summer 2018 and 2019 at UB site. We found
511 that the ending diameters slightly higher at UB site than MT site, but the difference is not
512 significant (49 nm vs 45 nm) as shown in Fig. R12c.

513 Earlier research has pointed out that in order to observe particle growth until 100 nm at a
514 measurement station under typical conditions, simultaneous NPF should happen over a very
515 large area (e.g. with wind speed 5 m/s and growth rate of 3 nm/h from the station to roughly
516 600 km upwind from the station) (Paasonen et al., 2018). During our observation in summer
517 2018 and 2019, most of the newly formed modes kept growing for about 20 hours after an
518 NPF event started, and the maximum horizontal extension of the observed NPF events in the
519 growth stage is restricted to within about 200 km ($\sim 2^\circ$ in latitude) north of UB site (Fig. 13).
520 As shown in Fig.13, the population density is also higher within the area extending ~ 200 km
521 north than beyond this limit. Therefore, it seems that NPF events were limited to the regions
522 with some contribution from anthropogenic emissions during air mass transport from north to
523 Beijing. Roughly similar extent of the NPF area is also seen in other directions. However,
524 towards the south it is more likely that increasing condensation sink from accumulating
525 pollution becomes the limiting factor for NPF occurrence rather than decreasing strength in
526 emission sources. NPF events at MT station had similar characteristics as those at UB station
527 with the NPF event region extending a few hundred kilometers towards the north. The NPF
528 events in this direction were disrupted after a relatively similar distance (or they enter the
529 growth stagnation phase, which will be discussed in section 3.6.3). The limited NPF event
530 area could possibly explain why most End Dp we observed were smaller than 70 nm.

531 *3.5 Effect of topography*

532 In Figure 14 we show average particle number size distribution and particle number
533 concentration on NPF event and non-event days during our short-term parallel observation at

534 both sites. On NPF event days, nucleation and Aitken mode particle number concentrations
535 were much smaller at MT station than those at UB station due to smaller particle formation
536 rates and less anthropogenic emissions. Interestingly, accumulation mode particle number
537 concentrations were higher at MT station ($701\text{-}2900\text{ cm}^{-3}$, with a median of 1500 cm^{-3}) than
538 that at UB station ($350\text{-}1416\text{ cm}^{-3}$ with a median of 700 cm^{-3}) (Fig.14b). Due to the close
539 proximity of the two measurement sites, the air mass arrival directions and source regions
540 were (mostly) similar at both sites throughout the measurement period, hence the regional
541 and transported cannot explain the higher accumulation mode particle number concentration
542 at MT site. As there were few primary emissions at MT site, the accumulation mode particles
543 could be attributed to secondary particles (Kulmala et al., 2021), indicating particles at MT
544 station were more aged than those at UB station (Fig.14a). The possible reasons is that
545 mountains block pollution diffusion, which in the end resulted in comparable CS at MT
546 station as UB station.

547 Figure 15 shows an example of the wind distribution before and during NPF event on June
548 30, 2019 at 850 hPa (close to the altitude of MT station) and 10 m above ground level. As
549 shown in Fig.15, the reanalyzed wind directions at 850 hPa were similar as those at 10 m
550 above the ground level at MT station. Actually, the wind conditions on other NPF event days
551 at MT station during our observation had similar characteristics that the wind directions were
552 similar between 850 hPa and 10 m above ground level indicating air masses well mixed
553 during NPF events. Earlier observations also found NPF event happened uniformly within the
554 mixing layer at their observation stations and particle number size distribution remains
555 roughly constant within the mixing layer (Shen et al., 2018;Lampilahti et al., 2021).

556 **3.6 case studies**

557 *3.6.1 Non-local NPF events at MT station*

558 As we discussed above, NPF events at MT stations were favored by strong photochemistry
559 (sufficient solar radiation) and low CS. However, we also observed two NPF events under
560 low solar radiation and high CS on June 15 and 25. These two NPF events had similar

561 characteristics, and we explain the case on June 15 in detail. During this case, air masses
562 arrived at both stations from south-east around 9:00 LT as shown in Fig. 16b&d, resulting in
563 high CS especially at MT and UB stations (Fig. 16a&c). The NPF event at the UB station was
564 observed around 11:00 LT, with a high median J_7 of $5.56 \text{ cm}^{-3}\text{s}^{-1}$, whereas no indication of
565 NPF event at MT was observed until 15:00 likely due to the high CS. After 15:00 LT, a new
566 growing mode from 15 nm appeared at MT station. Because there was no intense increase of
567 sub-15 nm particle number concentration throughout the whole event, the NPF event at MT
568 station was not local but occurred somewhere else and transported to MT station. This a
569 common phenomenon, particularly when the conditions do not favor NPF events to occur on
570 site, but are NPF-favorable somewhere else. The particles formed off-site are transported
571 vertically or horizontally and observed on site (Dada et al., 2018;Leino et al., 2019). Different
572 from other NPF events, this non-local NPF event was associated with strong southerly wind
573 (Fig. 16e), the NPF event observed at the MT station might originate from urban areas 60 km
574 south to the station as shown in Fig.1, assuming the NPF event started around 9:00 and the
575 mean wind speed was 3 m/s.

576 *3.6.2 Undefined day under low CS and high UV at MT station*

577 Interestingly, we also observed an undefined day at MT station with low CS (0.006 s^{-1}) and
578 high UV (28 W/m^2) on June 28 (Fig. 17c) as there seems to be a very weak ‘banana’ around
579 13:00 in the particle number size distribution plot. All other days with such conditions were
580 classified as NPF event days. In this case, the reasonable explanation would be low precursor
581 vapours which we think are SO_2 in our case. On this day, an air mass from Inner-Mongolia
582 arrived at both stations, resulting in very low SO_2 concentration at the UB station among all
583 NPF event days during our observation as shown in Fig. 4. It is reasonable to assume that the
584 SO_2 concentration was even lower at the MT station than at the UB station, and low H_2SO_4
585 concentration could also be expected, which could be insufficient to trigger an NPF event.
586 This is consistent with an earlier long-term observation at Shangdianzi, another background
587 site of Beijing, where the NPF events were suppressed by air masses from Inner-Mongolia
588 due to the low precursor concentrations (Shen et al., 2018). In comparison, we observed a

589 very weak NPF event at UB station at the same day, as local emissions were enough to supply
590 enough vapors to initiate NPF event.

591 *3.6.3 Growth stagnant and shrinkage case during our observation*

592 During our observations in summer 2018 and 2019 at urban site and the observation from
593 June 14 to July 14, 2019 at MT site, there were some cases where the newly-formed particles
594 entered a phase of growth stagnation or even displayed a decreasing mode diameter. On June
595 30, 2019 such case occurred simultaneously at both sites and we chose this day for a case
596 study.

597 As shown in Fig.18 a&b, the newly-formed particles entered a phase of growth stagnation
598 almost at the same time around 12:00 at both sites. Particle mode diameters decreased from
599 31 nm to 15 nm at UB station around 15:00, under relatively calm meteorological condition
600 indicating meteorological condition could not be the reason for particle sizes decrease on
601 June 30, 2019 at UB site. Around the same time, mode diameter at MT station also decreased
602 gradually from 25 nm to 16 nm. Earlier observations in summer-time Beijing have speculated
603 mode diameter decrease to be related to particle evaporation, which is triggered by favorable
604 meteorological conditions and vapor dilution (Zhang et al., 2016). From Fig.13, we see, that
605 the air masses observed during the growth stagnation or diameter decrease (both marked
606 under growth stagnation in the figure) were often located quite far in the north over the less
607 populated areas during the onset time of regional NPF. It is also possible, that the less
608 favorable initial conditions for particle formation and growth over these areas, combined with
609 increasing wind speed or temporal changes in the growth rate, could explain the observations
610 of decreasing particle sizes without evaporation (Kivekäs et al., 2016; Hakala et al., 2019).

611 **4 Summary and conclusions**

612 We conducted observations of NPF events at an urban site (UB) and a background mountain
613 site (MT) in Beijing and fully analyzed the favorable conditions for NPF event occurrences at
614 each of the sites. In order to identify the similarities and differences between NPF events at
615 both stations in terms of frequency, intensity and mechanisms, we compared certain NPF
616 characteristics including particle formation rate, growth rate as well as NPF event start time

617 and ending diameters of newly-formed growing particles at both stations. We found that NPF
618 events are most of the time a regional phenomenon occurring over the studied areas and
619 connected closely with air masses source regions during our observation. The air masses from
620 north favored common NPF events more than any other mass trajectories due to their
621 associated clean air masses and thus low CS. Additionally, air masses from the north group
622 always resulted in an NPF event at UB station, while other factors still suppressed their
623 occurrence at the MT station. For example, we found that sufficiently high solar radiation, e.g.
624 UV (UVA+UVB) intensity larger than 15 W/m^2 is required for an NPF event to occur at MT
625 and NPF events observed under solar radiation conditions smaller than 15 W/m^2 were rather
626 transported NPF events from areas upwind to MT station. Another factor suppressing the
627 occurrence of NPF events at MT is the too low precursor gas concentrations (e.g. SO_2) which
628 was visible in MT rather than at UB. Moreover, we found that the CS limit for NPF event
629 occurrence at UB station was $\sim 0.032 \text{ s}^{-1}$, which is consistent with earlier observations in
630 urban Beijing. In comparison, at MT station the CS limit could be only $\sim 0.013 \text{ s}^{-1}$, above
631 which local-NPF events could possibly be suppressed associated with the lower SO_2
632 concentration.

633 Although NPF events could happen simultaneously at both stations, the NPF event strength
634 (particle formation rates) was significantly higher at UB than MT station, possibly due to
635 spatial inhomogeneity in the sources of aerosol precursor compounds as well as solar
636 radiation. In addition, the particle growth rates in size range of 7-15 nm were also slightly
637 higher at UB than MT station. Regional NPF events were observed to occur with the
638 horizontal extent within around 200 kilometers when air masses arriving at Beijing from the
639 north, as a result, only a few NPF events were observed to end with mode diameters larger
640 than 70 nm. The size of the area with NPF events upwind our observation seems to be
641 connected with population density that weaker NPF event was assumed to happen in less
642 populated areas.

643 Overall, our results highlight the importance of anthropogenic emissions for NPF events
644 occurrence and subsequently growth in north China plain during summer. However, there are

645 still some uncertainties due to the limited data set. For more robust knowledge on NPF events
646 in north China plain, long-term and more comprehensive observations on NPF events upwind
647 and downwind urban Beijing are important. Such observations can shed light into the
648 regionality of NPF events and the dynamical development of the aerosol population
649 influenced by radical chemistry in the plume of a megacity.

650 **Conflict of interest:** The authors declare no competing interests.

651 **Author contributions:** YZ, CY, YG, XY performed the measurements. YZ, SH, CY, YG, LD,
652 XY analyzed the data. YZ, CY, SH, LD wrote the manuscript. All authors reviewed the paper
653 and contributed to the scientific discussions.

654 **Data availability:** The data displayed in this manuscript will be available online at
655 zenodo.com once the manuscript is in its final publication format.

656 **Financial support:** This publication has been produced within the framework of the
657 EMME-CARE project, which has received funding from the European Union's Horizon 2020
658 Research and Innovation Programme (under grant agreement no. 856612) and the
659 Government of Cyprus. This research has also received funding from the European
660 Commission grant agreement no. 742206 ("ERC-ATM-GTP") as well as Academy of Finland
661 Projects 316114 & 311932. Simo Hakala acknowledges the doctoral programme in
662 Atmospheric Sciences (ATM-DP, University of Helsinki) for financial support. The sole
663 responsibility of this publication lies with the author. The European Union is not responsible
664 for any use that may be made of the information contained therein.

665

667 **5 References**

668 Cai, R., and Jiang, J.: A new balance formula to estimate new particle formation rate: reevaluating the
669 effect of coagulation scavenging, *Atmos Chem Phys*, 17, 12659-12675, 10.5194/acp-17-12659-2017,
670 2017.

671 Cai, R., Yang, D., Fu, Y., Wang, X., Li, X., Ma, Y., Hao, J., Zheng, J., and Jiang, J.: Aerosol surface
672 area concentration: a governing factor in new particle formation in Beijing, *Atmos Chem Phys*, 17,
673 12327-12340, 10.5194/acp-17-12327-2017, 2017.

674 Cai, R., Yan, C., Yang, D., Yin, R., Lu, Y., Deng, C., Fu, Y., Ruan, J., Li, X., Kontkanen, J., Zhang, Q.,
675 Kangasluoma, J., Ma, Y., Hao, J., Worsnop, D. R., Bianchi, F., Paasonen, P., Kerminen, V.-M., Liu, Y.,
676 Wang, L., Zheng, J., Kulmala, M., and Jiang, J.: Sulfuric acid-amine nucleation in urban Beijing,
677 *Atmospheric Chemistry and Physics Discussions*, 10.5194/acp-2020-1060, 2020.

678 Carnerero, C., Pérez, N., Reche, C., Ealo, M., Titos, G., Lee, H.-K., Eun, H.-R., Park, Y.-H., Dada, L.,
679 Paasonen, P., Kerminen, V.-M., Mantilla, E., Escudero, M., Gómez-Moreno, F. J., Alonso-Blanco, E.,
680 Coz, E., Saiz-Lopez, A., Temime-Roussel, B., Marchand, N., Beddows, D. C. S., Harrison, R. M.,
681 Petäjä, T., Kulmala, M., Ahn, K.-H., Alastuey, A., and Querol, X.: Vertical and horizontal distribution
682 of regional new particle formation events in Madrid, *Atmos Chem Phys*, 18, 16601-16618,
683 10.5194/acp-18-16601-2018, 2018.

684 Chu, B., Dada, L., Liu, Y., Yao, L., Wang, Y., Du, W., Cai, J., Daellenbach, K., Chen, X., Simonen, P.,
685 Zhou, Y., Deng, C., Fu, Y., Yin, R., Li, H., He, X.-C., Feng, Z., Yan, C., Kangasluoma, J., and Kulmala,
686 M.: Particle growth with photochemical age from new particle formation to haze in the winter of
687 Beijing, China, *Science of The Total Environment.*, 753, 10.1016/j.scitotenv.2020.142207, 2021.

688 Chu, B. W., Kerminen, V. M., Bianchi, F., Yan, C., Petäjä, T., and Kulmala, M.: Atmospheric new
689 particle formation in China, *Atmos Chem Phys*, 19, 115-138, <https://doi.org/10.5194/acp-19-115-2019>,
690 2019.

691 Dada, L., Paasonen, P., Nieminen, T., Buenrostro Mazon, S., Kontkanen, J., Peräkylä, O., Lehtipalo,
692 K., Hussein, T., Petäjä, T., Kerminen, V.-M., Bäck, J., and Kulmala, M.: Long-term analysis of
693 clear-sky new particle formation events and nonevents in Hyytiälä, *Atmos Chem Phys*, 17, 6227-6241,

694 10.5194/acp-17-6227-2017, 2017.

695 Dada, L., Chellapermal, R., Buenrostro Mazon, S., Paasonen, P., Lampilahti, J., Manninen, H. E.,
696 Junninen, H., Petäjä, T., Kerminen, V.-M., and Kulmala, M.: Refined classification and
697 characterization of atmospheric new-particle formation events using air ions, *Atmos Chem Phys*, 18,
698 17883-17893, 10.5194/acp-18-17883-2018, 2018.

699 Dada, L., Lehtipalo, K., Kontkanen, J., Nieminen, T., Baalbaki, R., Ahonen, L., Duplissy, J., Yan, C.,
700 Chu, B., Petäjä, T., Lehtinen, K., Kerminen, V.-M., Kulmala, M., and Kangasluoma, J.: Formation and
701 growth of sub-3-nm aerosol particles in experimental chambers, *Nat Protoc*, , 15, 1013-1040,
702 10.1038/s41596-019-0274-z, 2020a.

703 Dada, L., Ylivinkka, I., Baalbaki, R., Li, C., Guo, Y., Yan, C., Yao, L., Sarnela, N., Jokinen, T.,
704 Daellenbach, K. R., Yin, R., Deng, C., Chu, B., Nieminen, T., Kontkanen, J., Stolzenburg, D., Sipilä,
705 M., Hussein, T., Paasonen, P., Bianchi, F., Salma, I., Weidinger, T., Pikridas, M., Sciare, J., Jiang, J.,
706 Liu, Y., Petäjä, T., Kerminen, V.-M., and Kulmala, M.: Sources and sinks driving sulphuric acid
707 concentrations in contrasting environments: implications on proxy calculations, *Atmos. Chem. Phys.*
708 *Discuss.*, 10.5194/acp-2020-155, 2020b.

709 Dai, L., Wang, H., Zhou, L., An, J., Tang, L., Lu, C., Yan, W., Liu, R., Kong, S., Chen, M., Lee, S.,
710 and Yu, H.: Regional and local new particle formation events observed in the Yangtze River Delta
711 region, China, *Journal of Geophysical Research: Atmospheres*, 122, 2389-2402,
712 10.1002/2016jd026030, 2017.

713 Dal Maso, M., Kulmala, M., Riipinen, I., Wagner, R., Hussein, T., Aalto, P. P., and Lehtinen, K. E. J.:
714 Formation and growth of fresh atmospheric aerosols: eight years of aerosol size distribution data from
715 SMEAR II, Hyytiälä, Finland, *Boreal Environ Res*, 10, 323-336, 2005.

716 Deng, C., Cai, R., Yan, C., Zheng, J., and Jiang, J.: Formation and growth of sub-3 nm particles in
717 megacities: impact of background aerosols, *Faraday Discuss*, 10.1039/d0fd00083c, 2020a.

718 Deng, C., Fu, Y., Dada, L., Yan, C., Cai, R., Yang, D., Zhou, Y., Yin, R., Lu, Y., Li, X., Qiao, X., Fan,
719 X., Nie, W., Kontkanen, J., Kangasluoma, J., Chu, B., Ding, A., Kerminen, V. M., Paasonen, P.,
720 Worsnop, D. R., Bianchi, F., Liu, Y., Zheng, J., Wang, L., Kulmala, M., and Jiang, J.: Seasonal
721 Characteristics of New Particle Formation and Growth in Urban Beijing, *Environ Sci Technol*, 54,

722 8547-8557, 10.1021/acs.est.0c00808, 2020b.

723 Du, W., Dada, L., Zhao, J., Chen, X., Daellenbach, K. R., Xie, C., Wang, W., He, Y., Cai, J., Yao, L.,
724 Zhang, Y., Wang, Q., Xu, W., Wang, Y., Tang, G., Cheng, X., Kokkonen, T. V., Zhou, W., Yan, C., Chu,
725 B., Zha, Q., Hakala, S., Kurppa, M., Järvi, L., Liu, Y., Li, Z., Ge, M., Fu, P., Nie, W., Bianchi, F.,
726 Petäjä, T., Paasonen, P., Wang, Z., Worsnop, D. R., Kerminen, V.-M., Kulmala, M., and Sun, Y.: A 3D
727 study on the amplification of regional haze and particle growth by local emissions, *npj Climate and*
728 *Atmospheric Science*, 4, 10.1038/s41612-020-00156-5, 2021.

729 Ehn, M., Thornton, J.A., Kleist, E., Sipila, M., Junninen, H., Pullinen, I., Springer, M., Rubach, F.,
730 Tillmann, R., Lee, B., Lopez-Hilfiker, F., Andres, S., Acir, I.-H., Rissanen, M., Jokinen, T.,
731 Schobesberger, S., Kangasluoma, J., Kontkanen, J., Nieminen, T., Kurten, T., Nielsen, L. B.,
732 Jorgensen, S., Kjaergaard, H. G., Canagaratna, M., Maso, M. D., Berndt, T., Petaja, T., Wahner, A.,
733 Kerminen, V.-M., Kulmala, M., Worsnop, D. R., Wildt, J., and Mentel, T. F.: A large source of
734 low-volatility secondary organic aerosol, *Nature*, 506, 476–479., 2014.

735 Gao, Y., Zhang, D., Wang, J., Gao, H., and Yao, X.: Variations in Ncn and Nccn over China marginal
736 seas related to marine traffic emissions, new particle formation and aerosol aging, *Atmos. Chem.*
737 *Phys.*, in press 2020.

738 Guo, S., Hu, M., Zamora, M. L., Peng, J. F., Shang, D. J., Zheng, J., Du, Z. F., Wu, Z., Shao, M., Zeng,
739 L. M., Molina, M. J., and Zhang, R. Y.: Elucidating severe urban haze formation in China, *P Natl*
740 *Acad Sci USA*, 111, 17373-17378, 10.1073/pnas.1419604111, 2014.

741 Guo, S., Hu, M., Peng, J., Wu, Z., Zamora, M. L., Shang, D., Du, Z., Zheng, J., Fang, X., Tang, R.,
742 Wu, Y., Zeng, L., Shuai, S., Zhang, W., Wang, Y., Ji, Y., Li, Y., Zhang, A. L., Wang, W., Zhang, F.,
743 Zhao, J., Gong, X., Wang, C., Molina, M. J., and Zhang, R.: Remarkable nucleation and growth of
744 ultrafine particles from vehicular exhaust, *Proc Natl Acad Sci U S A*, 117, 3427-3432,
745 10.1073/pnas.1916366117, 2020.

746 Hakala, S., Alghamdi, M. A., Paasonen, P., Vakkari, V., Khoder, M. I., Neitola, K., Dada, L.,
747 Abdelmaksoud, A. S., Al-Jeelani, H., Shabbaj, I. I., Almeahadi, F. M., Sundström, A.-M., Lihavainen,
748 H., Kerminen, V.-M., Kontkanen, J., Kulmala, M., Hussein, T., and Hyvärinen, A.-P.: New particle
749 formation, growth and apparent shrinkage at a rural background site in western Saudi Arabia, *Atmos*

750 Chem Phys, 19, 19, <https://doi.org/10.5194/acp-19-10537-2019>, 2019.

751 Hamed, A., Korhonen, H., Sihto, S.-L., Joutsensaari, J., Järvinen, H., Petäjä, T., Arnold, F., Nieminen,
752 T., Kulmala, M., Smith, J. N., Lehtinen, K. E. J., Laaksonen, A., and High relative humidity suppresses
753 continental new particle formation events, 2010.

754 Hamed, A., Korhonen, H., Sihto, S.-L., Joutsensaari, J., Järvinen, H., Petäjä, T., Arnold, F., Nieminen,
755 T., Kulmala, M., Smith, J. N., Lehtinen, K. E. J., and Laaksonen, A.: The role of relative humidity in
756 continental new particle formation, *Journal of Geophysical Research*, 116, 10.1029/2010jd014186,
757 2011.

758 Herrmann, E., Ding, A. J., Kerminen, V. M., Petäjä, T., Yang, X. Q., Sun, J. N., Qi, X. M., Manninen,
759 H., Hakala, J., Nieminen, T., Aalto, P. P., Kulmala, M., and Fu, C. B.: Aerosols and nucleation in
760 eastern China: first insights from the new SORPES-NJU station, *Atmos Chem Phys*, 14, 2169-2183,
761 10.5194/acp-14-2169-2014, 2014.

762 Hussein, T., Junninen, H., Tunved, P., Kristensson, A., Dal Maso, M., Riipinen, I., Aalto, P. P.,
763 Hansson, H. C., Swietlicki, E., and Kulmala, M.: Time span and spatial scale of regional new particle
764 formation events over Finland and Southern Sweden, *Atmos Chem Phys*, 9, 4699-4716,
765 10.5194/acp-9-4699-2009, 2009.

766 Jun, Y.-S., Jeong, C.-H., Sabaliauskas, K., Richard Leitch, W., and Evans, G. J.: A year-long
767 comparison of particle formation events at paired urban and rural locations, *Atmospheric Pollution*
768 *Research*, 5, 447-454, 10.5094/apr.2014.052, 2014.

769 Kangasluoma, J., Cai, R., Jiang, J., Deng, C., Stolzenburg, D., Ahonen, L. R., Chan, T., Fu, Y., Kim,
770 C., Laurila, T. M., Zhou, Y., Dada, L., Sulo, J., Flagan, R. C., Kulmala, M., Petäjä, T., and Lehtipalo,
771 K.: Overview of measurements and current instrumentation for 1–10 nm aerosol particle number size
772 distributions, *J Aerosol Sci*, 148, 10.1016/j.jaerosci.2020.105584, 2020.

773 Kerminen, V. M., Chen, X. M., Vakkari, V., Petäjä, T., Kulmala, M., and Bianchi, F.: Atmospheric new
774 particle formation and growth: review of field observations, *Environ Res Lett*, 13,
775 <https://doi.org/10.1088/1748-9326/aadf3c>, 2018.

776 Komppula, M., Sihto, S.-L., Korhonen, H., Lihavainen, H., Kerminen, V.-M., Kulmala, M., and
777 Viisanen, Y.: New particle formation in air mass transported between two measurement sites in

778 Northern Finland, *Atmos Chem Phys*, 6, 14, www.atmos-chem-phys.net/6/2811/2006/, 2006.

779 Kontkanen, J., Deng, C., and Fu, Y., Dada, L., Zhou, Y., Cai, J., Daellenbach, R.-K., Hakala, S.,
780 Kokkonen, V.-T., Lin, Z., Liu, Y., Wang, Y., Yan, C., Petäjä, T., Jiang, J., Kulmala, M and Paasonen, P.:
781 Size-resolved particle number emissions in Beijing determined from measured particle size
782 distributions, *Atmos Chem Phys*, 20, 11329–11348, <https://doi.org/10.5194/acp-20-11329-2020>, 2020.

783 Kivekäs, N., Carpman, J., Roldin, P., Leppä, J., O’Connor, E., Kristensson, A., and Asmi, E.:
784 Coupling an aerosol box model with one-dimensional flow: a tool for understanding
785 observations of new particle formation events, *Tellus B*, 68, 29706,
786 [doi:10.3402/tellusb.v68.29706](https://doi.org/10.3402/tellusb.v68.29706), 2016.

787 Kristensson, A., Johansson, M., Swietlicki, E., Kivekäs, N., Hussein, T., Nieminen, T., Kulmala, M.,
788 and Dal Maso, M.: NanoMap: geographical mapping of atmospheric new particle formation through
789 analysis of particle number size distribution data, *Boreal Environ. Res.*, 19 (suppl. B), 329–342,
790 2014.

791 Kulmala, M., Petäjä, T., Nieminen, T., Sipilä, M., Manninen, H. E., Lehtipalo, K., Dal Maso, M.,
792 Aalto, P. P., Junninen, H., Paasonen, P., Riipinen, I., Lehtinen, K. E. J., Laaksonen, A., and Kerminen,
793 V. M.: Measurement of the nucleation of atmospheric aerosol particles, *Nat Protoc*, 7, 1651-1667,
794 <https://doi.org/10.1038/nprot.2012.091>, 2012.

795 Kulmala, M., Dada, L., Dällenbach, K., Yan, C., Stolzenburg, D., Kontkanen, J., Ezhova, E., Hakala,
796 S., Tuovinen, S., Kokkonen, T., Kurppa, M., Cai, R., Zhou, Y., Yin, R., Baalbaki, R., Chan, T., Chu, B.,
797 Deng, C., Fu, Y., Ge, M., He, H., Heikkinen, L., Junninen, H., Nei, W., Rusanen, A., Vakkari, V.,
798 Wang, Y., Wang, L., yao, I., Zheng, J., Kujansuu, J., Kangasluoma, J., Petäjä, T., Paasonen, P., Järvi,
799 L., Worsnop, D., Ding, A., Liu, Y., Jiang, J., Bianchi, F., Yang, G., Liu, Y., Lu, Y., and Kerminen,
800 V.-M.: Is reducing new particle formation a plausible solution to mitigate particulate air pollution in
801 Beijing and other Chinese megacities?, *Faraday Discuss*, 10.1039/d0fd00078g, 2021.

802 Lampilahti, J., Manninen, H. E., Nieminen, T., Mirme, S., Ehn, M., Pullinen, I., Leino, K.,
803 Schobesberger, S., Kangasluoma, J., Kontkanen, J., Järvinen, E., Väänänen, R., Yli-Juuti, T., Krejci,
804 R., Lehtipalo, K., Levula, J., Mirme, A., Decesari, S., Tillmann, R., Worsnop, D. R., Rohrer, F.,
805 Kiendler-Scharr, A., Petäjä, T., Kerminen, V.-M., Mentel, T. F., and Kulmala, M.: Zeppelin-led study

806 on the onset of new particle formation in the planetary boundary layer, *Atmospheric Chemistry and*
807 *Physics Discussions*, 10.5194/acp-2021-282, 2021.

808 Lehtipalo, K., Leppä, J., Kontkanen, J., Kangasluoma, J., Wimmer, D., Franchin, A., Schobesberger,
809 S., Junninen, H., Petäjä, T., Sipilä, M., Mikkilä, J., Vanhanen, J., Worsnop, D. r., and Kulmala, M.:
810 methods for determining particle size distribution and growth rates between 1 and 3 nm using the
811 Particle Size Magnifier, *Boreal Environ Res*, 19 215-236, 2014.

812 Lehtipalo, K., Yan, C., Dada, L., Bianchi, F., Xiao, M., Wagner, R., Stolzenburg, D., Ahonen, L. R.,
813 Amorim, A., Baccharini, A., Bauer, P. S., Baumgartner, B., Bergen, A., Bernhammer, A. K.,
814 Breitenlechner, M., Brilke, S., Buchholz, A., Mazon, S. B., Chen, D. X., Chen, X. M., Dias, A.,
815 Dommen, J., Draper, D. C., Duplissy, J., Ehn, M., Finkenzeller, H., Fischer, L., Frege, C., Fuchs, C.,
816 Garmash, O., Gordon, H., Hakala, J., He, X. C., Heikkinen, L., Heinritzi, M., Helm, J. C., Hofbauer,
817 V., Hoyle, C. R., Jokinen, T., Kangasluoma, J., Kerminen, V. M., Kim, C., Kirkby, J., Kontkanen, J.,
818 Kurten, A., Lawler, M. J., Mai, H. J., Mathot, S., Mauldin, R. L., Molteni, U., Nichman, L., Nie, W.,
819 Nieminen, T., Ojdanic, A., Onnela, A., Passananti, M., Petäjä, T., Piel, F., Pospisilova, V., Quéléver, L.
820 L. J., Rissanen, M. P., Rose, C., Sarnela, N., Schallhart, S., Schuchmann, S., Sengupta, K., Simon, M.,
821 Sipilä, M., Tauber, C., Tomé, A., Tröstl, J., Väisänen, O., Vogel, A. L., Volkamer, R., Wagner, A. C.,
822 Wang, M. Y., Weitz, L., Wimmer, D., Ye, P. L., Ylisirnio, A., Zha, Q. Z., Carslaw, K. S., Curtius, J.,
823 Donahue, N. M., Flagan, R. C., Hansel, A., Riipinen, I., Virtanen, A., Winkler, P. M., Baltensperger,
824 U., Kulmala, M., and Worsnop, D. R.: Multicomponent new particle formation from sulfuric acid,
825 ammonia, and biogenic vapors, *Sci Adv*, 4, <https://doi.org/10.1126/sciadv.aau5363>, 2018.

826 Leino, K., Lampilahti, J., Poutanen, P., Väänänen, R., Manninen, A., Buenrostro Mazon, S., Dada, L.,
827 Franck, A., Wimmer, D., Aalto, P. P., Ahonen, L. R., Enroth, J., Kangasluoma, J., Keronen, P.,
828 Korhonen, F., Laakso, H., Matilainen, T., Siivola, E., Manninen, H. E., Lehtipalo, K., Kerminen,
829 V.-M., Petäjä, T., and Kulmala, M.: Vertical profiles of sub-3 nm particles over the boreal
830 forest, *Atmos Chem Phys*, 19, 4127-4138, 10.5194/acp-19-4127-2019, 2019.

831 Liu, J., Zhang, X. L., Xu, X. F., and Xu, H. H.: Comparison analysis of variation characteristics of
832 SO₂, NO_x, O₃ and PM_{2.5} between rural and urban areas, *Beijing Huan jing ke xue= Huanjing kexue*
833 / [bian ji, Zhongguo ke xue yuan huan jing ke xue wei yuan hui "Huan jing ke xue" bian ji wei yuan

834 hui.], 29, 1059-1065, 2008.

835 Liu, J. Q., Jiang, J. K., Zhang, Q., Deng, J. G., and Hao, J. M.: A spectrometer for measuring particle
836 size distributions in the range of 3 nm to 10 μ m, *Front Env Sci Eng*, 10, 63-72,
837 <https://doi.org/10.1007/s11783-014-0754-x>, 2016.

838 Lee, B. P., Li, Y. J., Flagan, R. C., Lo, C., and Chan, C. K.: Sizing characterization of the fast mobility
839 particle sizer (FMPS) against SMPS and HR-ToF-AMS, *Aerosol Sci. Technol.*, 47, 1030–1037,
840 <https://doi.org/10.1080/02786826.2013.810809>, 2013.

841 Lu, Y., Yan, C., Fu, Y., Chen, Y., Liu, Y., Yang, G., , Wang, Y., Bianchi, F., Chu, B., and Zhou, Y.: A
842 proxy for atmospheric daytime gaseous sulfuric acid concentration in urban Beijing, *Atmos Chem*
843 *Phys*, 19, 1971-1983, 10.5194/acp-19-1971-2019, 2019.

844 Ma, L., Zhu, Y., Zheng, M., Sun, Y., Huang, L., Liu, X., Gao, Y., Shen, Y., Gao, H., and Yao, X.:
845 Investigating three patterns of new particles growing to the size of cloud condensation nuclei in
846 Beijing's urban atmosphere, *Atmos Chem Phys*, 21, 183-200, 10.5194/acp-21-183-2021, 2021.

847 Man, H. Y., Zhu, Y. J., Ji, F., Yao, X. H., Lau, N. T., Li, Y. J., Lee, B. P., and Chan, C. K.: Comparison
848 of Daytime and Nighttime New Particle Growth at the HKUST Supersite in Hong Kong, *Environ Sci*
849 *Technol*, 49, 7170-7178, 2015.

850 Olauson, J.: ERA5: The new champion of wind power modelling?, *Renewable Energy*, 126, 322-331,
851 2018.

852 Paasonen, P., Peltola, M., Kontkanen, J., Junninen, H., Kerminen, V.-M., and Kulmala, M.:
853 Comprehensive analysis of particle growth rates from nucleation mode to cloud condensation nuclei
854 in boreal forest, *Atmos Chem Phys*, 18, 12085-12103, 10.5194/acp-18-12085-2018, 2018.

855 Pierce, J. R., and Adams P. J.: Uncertainty in global CCN concentrations from uncertain
856 aerosol nucleation and primary emission rates. *Atmos. Chem. Phys.*, 9,
857 1339–1356, 10.5194/acp-9-1339-2009, 2009.

858 Qi, X., Ding, A., Roldin, P., Xu, Z., Zhou, P., Sarnela, N., Nie, W., Huang, X., Rusanen, A., Ehn, M.,
859 Rissanen, M. P., Petäjä, T., Kulmala, M., and Boy, M.: Modelling studies of HOMs and their
860 contributions to new particle formation and growth: comparison of boreal forest in Finland and a
861 polluted environment in China, *Atmos Chem Phys*, 18, 11779-11791, 10.5194/acp-18-11779-2018,

862 2018.

863 Qi, X. M. D., A. J., Nie, W., Petaja, T., Kerminen, V. M., Herrmann, E., Xie, Y. N., Zheng, L. F.,
864 Manninen, H., Aalto, P., Sun, J. N., Xu, Z. N., Chi, X. G., Huang, X., Boy, M., Virkkula, A., Yang, X.
865 Q., Fu, C. B., and Kulmala, M.: Aerosol size distribution and new particle formation in the western
866 Yangtze River Delta of China: 2 years of measurements at the SORPES station, *Atmos Chem Phys*, 15,
867 12445-12464, 2015.

868 Salma, I., Borsós, T., Weidinger, T., Aalto, P., Hussein, T., Dal Maso, M., and Kulmala, M.:
869 Production, growth and properties of ultrafine atmospheric aerosol particles in an urban environment.
870 *Atmospheric Chemistry and Physics*. 11. 10.5194/acp-11-1339-2011,2011.

871 Salma, I., Németh, Z., Kerminen, V.-M., Aalto, P., Nieminen, T., Weidinger, T., Molnár, Á., Imre, K.,
872 and Kulmala, M.: Regional effect on urban atmospheric nucleation, *Atmos Chem Phys*, 16,
873 8715-8728, 10.5194/acp-16-8715-2016, 2016.

874 Shen, X., Sun, J., Kivekäs, N., Kristensson, A., Zhang, X., Zhang, Y., Zhang, L., Fan, R., Qi, X., Ma,
875 Q., and Zhou, H.: Spatial distribution and occurrence probability of regional new particle formation
876 events in eastern China, *Atmos Chem Phys*, 18, 587-599, 10.5194/acp-18-587-2018, 2018.

877 Shen, X. J., Sun, J. Y., Zhang, Y. M., Wehner, B., Nowak, A., Tuch, T., Zhang, X. C., Wang, T. T.,
878 Zhou, H. G., Zhang, X. L., Dong, F., Birmili, W., and Wiedensohler, A.: First long-term study of
879 particle number size distributions and new particle formation events of regional aerosol in the North
880 China Plain, *Atmos Chem Phys*, 11, 1565-1580, 2011.

881 Stohl, A., Forster, C., Frank, A., Seibert, P., and Wotawa, G.: Technical note: The Lagrangian particle
882 dispersion model FLEXPART version 6.2. , *Atmospheric Chemistry and Physics*,5, 24,
883 10.5194/acp-5-2461-2005., 2005.

884 Vana, M., Komsaare, K., Hörrak, U., Mirme, S., Nieminen, T., Petäjä, T., Noe, S. M., Kontkanen, J.,
885 Manninen, H. E., , and Kulmala, M.: Characteristics of new-particle formation at three SMEAR
886 stations, *Boreal Environ Res*, 21, 17, 2016.

887 Wang, J., Shen, Y., Li, K., Gao, Y., Gao, H., and Yao, X.: Nucleation-mode particle pool and large
888 increases in Ncn and Nccn observed over the northwestern Pacific Ocean in the spring of 2014. ,
889 *Atmos. Chem. Phys.*, 19, 17, <https://doi.org/10.5194/acp-19-8845-2019>, 2019.

890 Wang, M., Zhu, T., Zhang, J. P., Zhang, Q. H., Lin, W. W., Li, Y., and Wang, Z. F.: Using a mobile
891 laboratory to characterize the distribution and transport of sulfur dioxide in and around Beijing, *Atmos*
892 *Chem Phys*, 11, 11631-11645, 2011.

893 Wang, Z. B., Hu, M., Sun, J. Y., Wu, Z. J., Yue, D. L., Shen, X. J., Zhang, Y. M., Pei, X. Y., Cheng, Y.
894 F., and Wiedensohler, A.: Characteristics of regional new particle formation in urban and regional
895 background environments in the North China Plain, *Atmos Chem Phys*, 13, 12495-12506,
896 10.5194/acp-13-12495-2013, 2013.

897 Wang, Z. B., Wu, Z. J., Yue, D. L., Shang, D. J., Guo, S., Sun, J. Y., Ding, A. J., Wang, L., Jiang, J. K.,
898 Guo, H., Gao, J., Cheung, H. C., Morawska, L., Keywood, M., and Hu, M.: New particle formation in
899 China: Current knowledge and further directions, *Science of the Total Environment*, 577, 258-266,
900 2017.

901 Wu, Z., Hu, M., Liu, S., Wehner, B., Bauer, S., Maßling, A., Wiedensohler, A., Petäjä, T., Dal Maso,
902 M., and Kulmala, M.: New particle formation in Beijing, China: Statistical analysis of a 1-year data
903 set, *Journal of Geophysical Research*, 112, 10.1029/2006jd007406, 2007.

904 Yang-Chun, Y., Bo, H., and Wang, Y.: Changing Characteristics of the Main Air Pollutants of the
905 Dongling Mountain in Beijing, *Environmental Science*, 34, 8, 2013.

906 Yao, L., Garmash, O., Bianchi, F., Zheng, J., Yan, C., Kontkanen, J., Junninen, H., Mazon, S. B., Ehn,
907 M., Paasonen, P., Sipilä, M., Wang, M. Y., Wang, X. K., Xiao, S., Chen, H. F., Lu, Y. Q., Zhang, B. W.,
908 Wang, D. F., Fu, Q. Y., Geng, F. H., Li, L., Wang, H. L., Qiao, L. P., Yang, X., Chen, J. M., Kerminen,
909 V. M., Petäjä, T., Worsnop, D. R., Kulmala, M., and Wang, L.: Atmospheric new particle formation
910 from sulfuric acid and amines in a Chinese megacity, *Science*, 361, 278-281,
911 <https://doi.org/10.1126/science.aao4839>, 2018.

912 Yao, L., Fan, X., Yan, C., Kurtén, T., Daellenbach, K. R., Li, C., Wang, Y., Guo, Y., Dada, L., and
913 Rissanen, M. P., Cai, J., Tham, Y. J., Zha, Q., Zhang, S., Du, W., Yu, M., Zheng, F., Zhou, Y.,
914 Kontkanen, J., Chan, T., Shen, J., Kujansuu, J. T., Kangasluoma, J., Jiang, J., Wang, L., Worsnop, D.
915 R., Petäjä, T., Kerminen, V.-M., Liu, Y., Chu, B., He, H., Kulmala, M., and Bianchi, F.:
916 Unprecedented Ambient Sulfur Trioxide (SO₃) Detection: Possible Formation Mechanism and
917 Atmospheric Implications, *Environ Sci Tech Let* 7, 809-818, 10.1021/acs.estlett.0c00615, 2020.

918 Ying, G, Ma, J., and Xing, Y.: Comparison of air quality management strategies of PM10, SO2, and
919 NOx by an industrial source complex model in Beijing, *Environmental Progress*, 26, 33-42, 2010.

920 Yu, F. and Luo, G.: Simulation of particle size distribution with a global aerosol model:
921 contribution of nucleation to aerosol and CCN number concentrations, *Atmos. Chem. Phys.*,
922 9, 7691–7710, 10.5194/acp-9-7691-2009, 2009.

923 Zhang, J., Chen, Z., Lu, Y., Gui, H., Liu, J., Wang, J., Yu, T., and Cheng, Y.: Observations of New
924 Particle Formation, Subsequent Growth and Shrinkage during Summertime in Beijing, *Aerosol Air*
925 *Qual Res*, 16, 1591-1602, 10.4209/aaqr.2015.07.0480, 2016.

926 Zhou, Y., Dada, L., Liu, Y., and Fu, Y., Kangasluoma, J., Chan, T., Yan, C., Chu, B., Daellenbach, K.
927 R., Bianchi, F., Kokkonen, T. V., Liu, Y., Kujansuu, J., Kerminen, V.-M., Petäjä, T., Wang, L., Jiang, J.,
928 and Kulmala, M.: Variation of size-segregated particle number concentrations in wintertime Beijing,
929 *Atmos Chem Phys*, 20, 1201-1216 10.5194/acp-20-1201-2020, 2020.

930 Zimmerman, N., Jeong, C.-H., Wang, J. M., Ramos, M., Wallace, J. S., and Evans, G. J.: A
931 source-independent empirical correction procedure for the fast mobility and engine exhaust particle
932 sizers, *Atmos. Environ.*, 100, 7, 838 10.1016/j.atmosenv.2014.10.054, 2015., 2015.

933

934

935

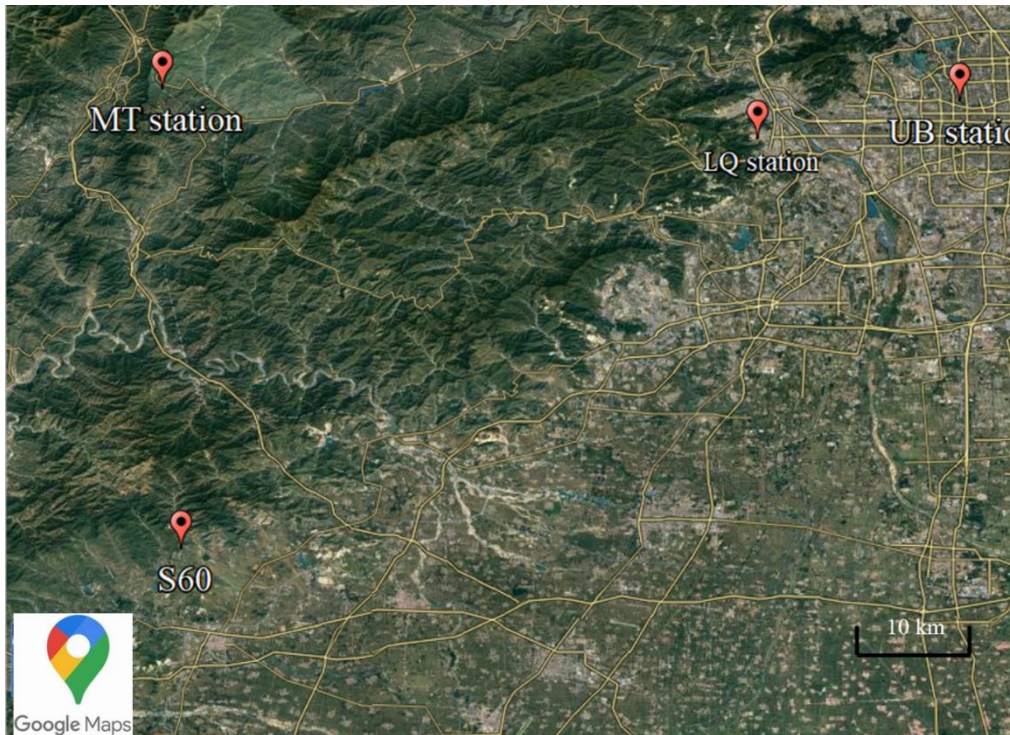
937 **Table 1:** NPF event and non- event days during our observation at both stations.

Date	Type	Air masses (9:00-15:00)		GR _{7-15nm} (nm/h)		J ₇ (cm ⁻³ s ⁻¹)		Event Start (LT)		Ending diameter (nm)	
		UB	MT	UB	MT	UB	MT	UB	MT	UB	MT
2019/06/14	a	North	North	8.61	-	4.97	-	9:00	8:00	71	-
2019/06/15*	a	Local	Local	12.63	-	5.56	-	11:00	15:00	82	60
2019/06/17	d	East	Local								
2019/06/18	c	Local	West		10.5		0.17		12:00		45
2019/06/19	d	South	Local								
2019/06/21	d	East	Local								
2019/06/23	e	East	East								
2019/06/24	f	Local	Local		8.21		-		12:00		50
2019/06/25*	a	Local	Local	-	-	-	-	12:00	15:00	-	53
2019/06/28	g	West	West	-		-		11:00			
2019/06/29	a	North	North	12.93	7.14	6.93	2.28	9:00	8:00	21	19
2019/06/30	a	North	North	4.82	6.57	9.86	1.37	6:30	9:30	31	25
2019/07/01	a	North	North	7.31	5.82	3.84	0.82	9:00	8:30	105	102
2019/07/02	d	Local	West								
2019/07/03	a	North	North	7.89	6.52	3.25	0.75	9:00	8:00	72	46
2019/07/04	b	Local	Local	-		-		10:00		53	
2019/07/06	a	North	North	7.39	6.51	9.21	1.75	7:00	9:30	25	19
2019/07/07	b	North	North	7.61		3.61		9:00		32	
2019/07/08	d	East	East								
2019/07/09	d	East	East								
2019/07/10	h	East	East								
2019/07/11	d	East	East								

2019/07/12	f	East	East		5.57		0.37		9:30		24
2019/07/13	c	Local	North		6.32		0.70		10:00		30
2019/07/14	a	North	North	12.04	9.86	3.91	0.89	9:30	9:30	63	47

938 'a' means NPF event observed at both stations, 'b' means NPF event day at UB station while
939 non-event day at MT station, 'c' means NPF event day at MT station while non-event day at UB
940 station, 'd' means non-event day at both stations on the same day, 'e' means undefined day at both
941 stations, 'f' means undefined day at UB station while NPF event day at MT station, g means
942 undefined day at MT station while NPF event day at UB station, h means undefined day at UB station
943 while non-event day at MT station, * means NPF event observed at MT station was transported from
944 somewhere else. – means the values cannot be reliably calculated. Only days when particle number
945 size distribution were valid are included in this table.

946

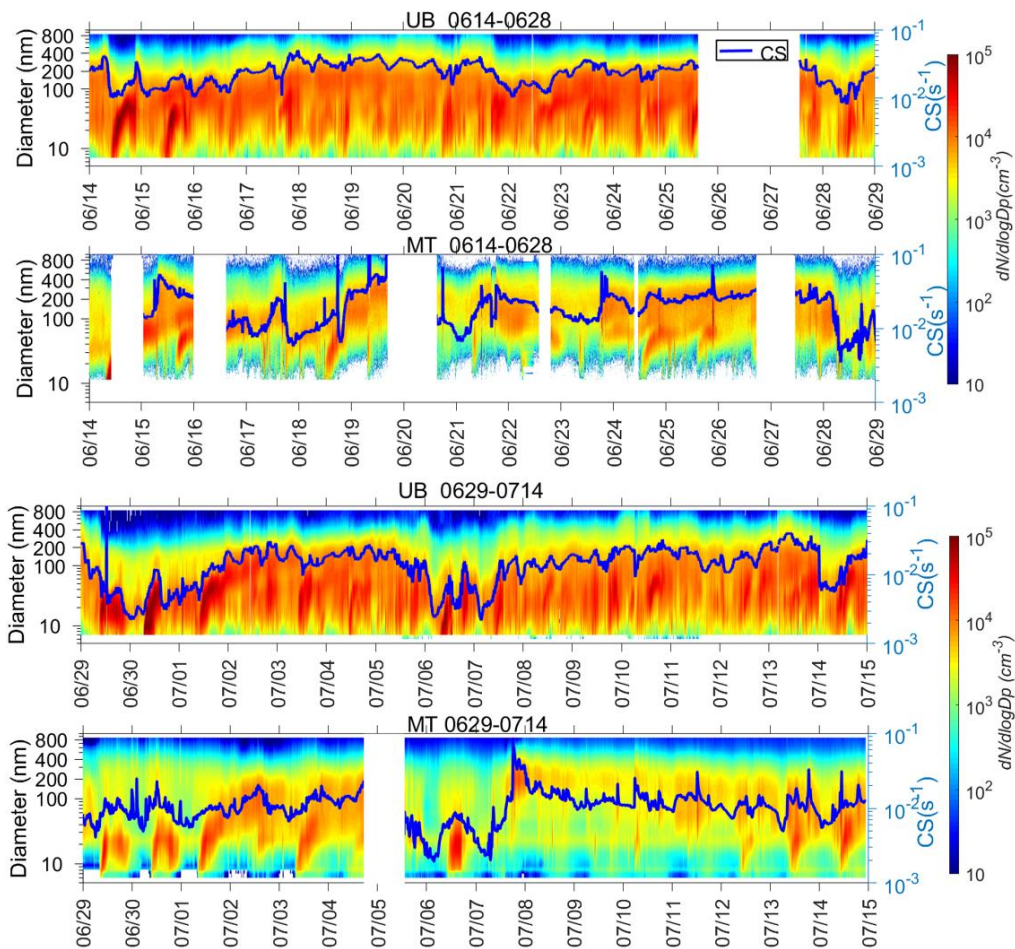


947

948 **Figure 1:** Map showing locations of urban station (UB), Longquan station (LQ), mountain
949 station (MT) and another site 60 km south from MT station (S60). The S60 referred to the
950 location where particles formed during the non-local NPF event observed at MT station on
951 June 15, 2019. Image is produced using © Google Maps.

952

953

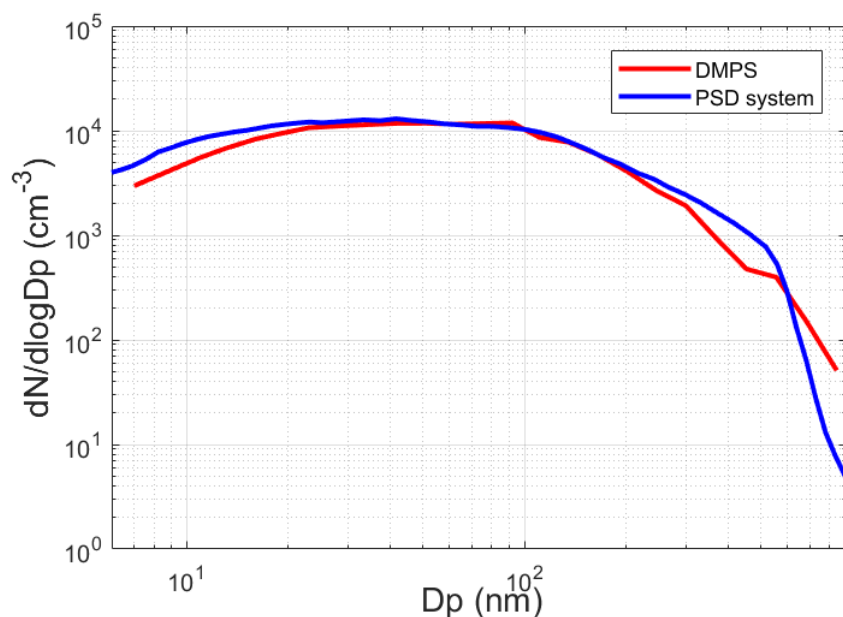


954

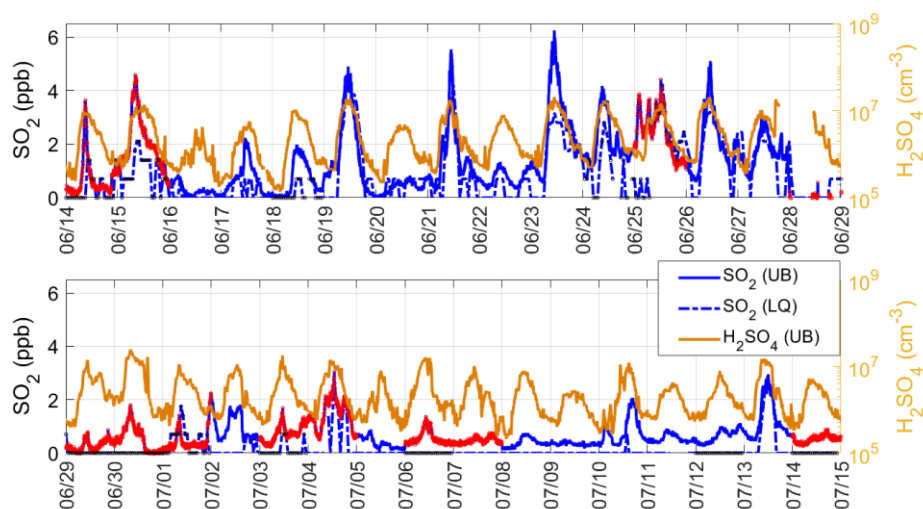
955 **Figure 2:** Time series of particle number size distribution and CS (the blue line) at UB and
 956 MT stations during our observations. Time resolutions for particle number size distribution
 957 data and CS were 8 min at UB station and 4 min at MT station, respectively.

958

959

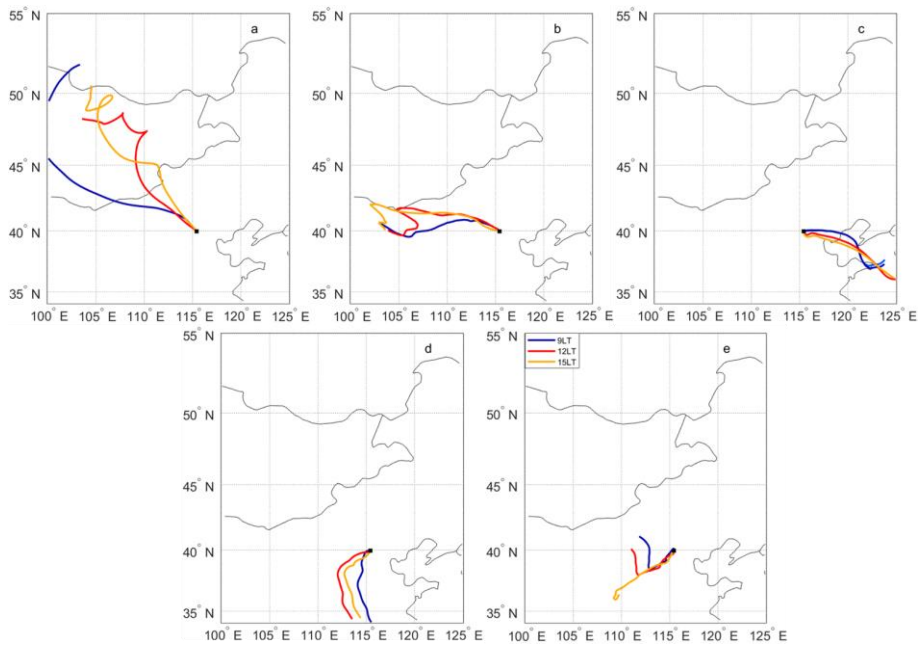


960
 961 **Figure 3:** Median particle number size distribution in 5-900 nm measured by DMPS and PSD
 962 during our observation from June 1 to August 31, 2019 at UB station. The time window of
 963 the data is from 9:00-15:00 of every day.



964
 965 **Figure 4:** Time series of SO₂ concentration (ppb) at UB station and Longquan station (LQ)
 966 during our observation (left axis) as well as H₂SO₄ concentration measured at UB station
 967 (right axis). Data under detection limit are set as zero at both stations. Data on NPF event
 968 days were marked in red at UB station and black at MT station. Time resolution for SO₂ data
 969 was 5 min at UB station and 1h at LQ station, respectively.

970



971

972 **Figure 5:** Examples of air masses arrived at both stations from (a) North group, (b) West

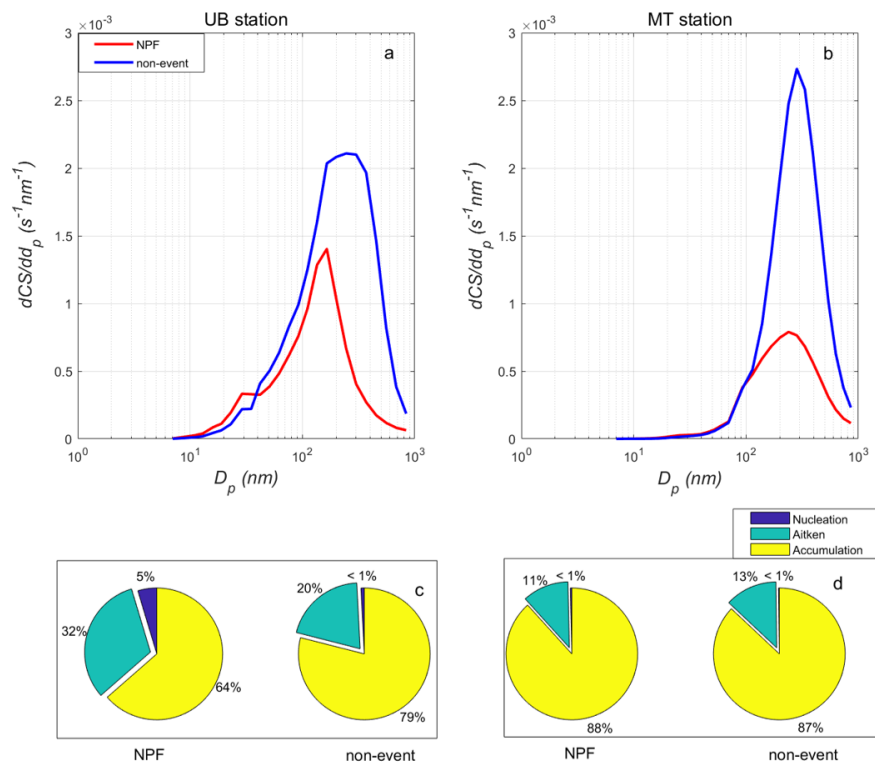
973 group, (c) East group, (d) South group and (d) Local group during 9:00-15:00 (local time, LT).

974 Both stations are under the same marker.

975

976

977

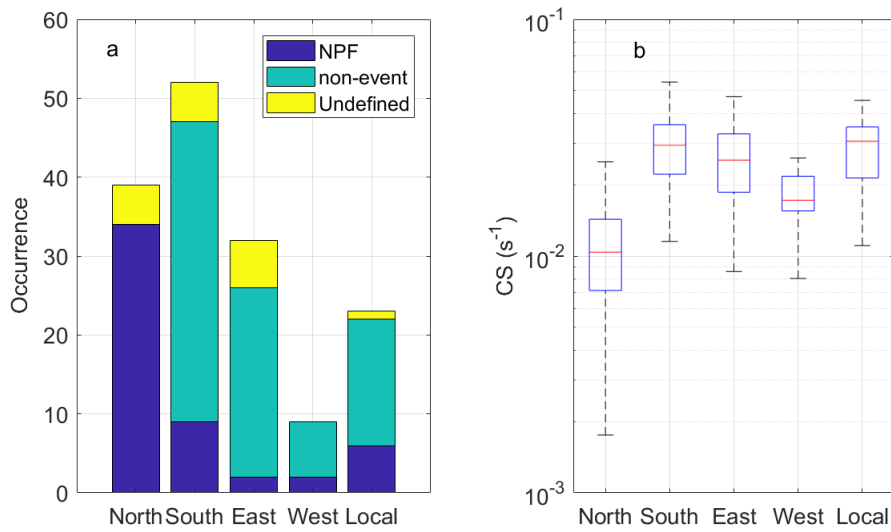


978

979 **Figure 6:** Median CS size distribution at UB (a) and MT (b) stations on NPF event and
 980 non-event days, respectively during 9:00-15:00 (local time, LT) and median contribution of
 981 nucleation, Aitken and accumulation mode particles to total CS at UB (c) and MT (d) stations
 982 on NPF event and non-event days, respectively during 9:00-15:00 (local time, LT). The
 983 time resolutions for CS and particle number concentration data were 8 min at UB station and
 984 4 min at MT station, respectively.

985

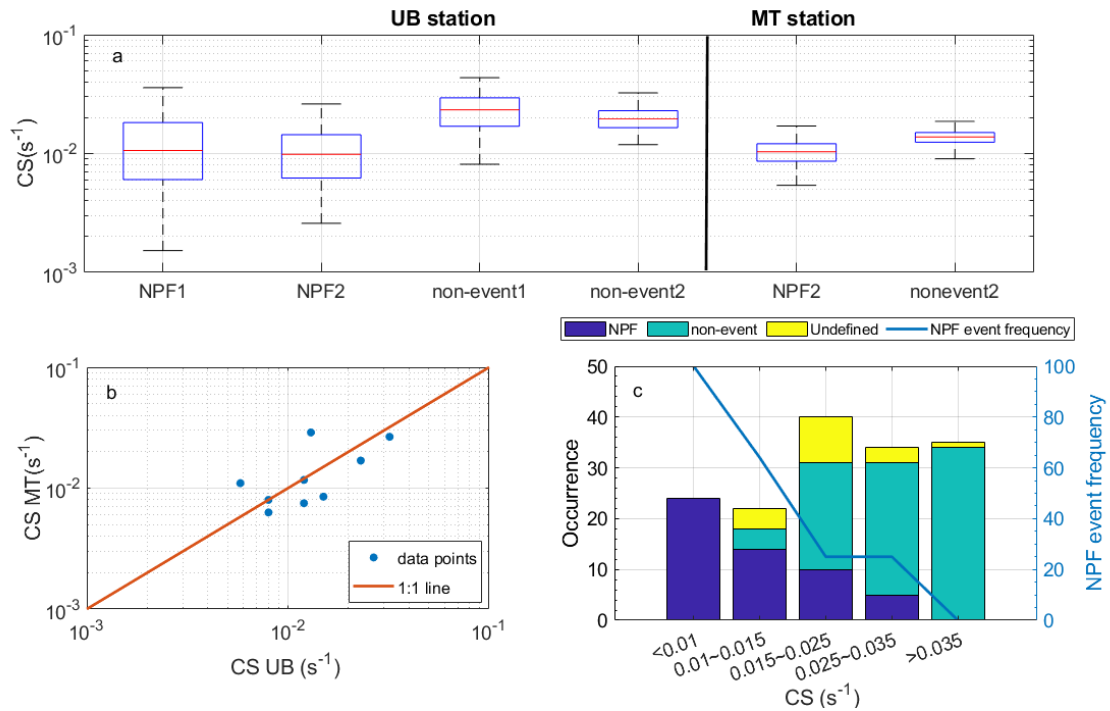
986



987

988 **Figure 7:** Occurrence of NPF events and non-events under air masses arriving from different
 989 directions (a) as well as medians and percentiles of condensation sink (CS, s^{-1}) during the
 990 9:00-11:00 (local time) under different air masses (b) during our observation in summer 2018
 991 and 2019 at UB station. The red line represents the median of the data and the lower and
 992 upper edges of the box represent 25th and 75th percentiles of the data, respectively. The length
 993 of the whiskers represents $1.5 \times$ interquartile range which includes 99.3% of the data. Data
 994 outside the whiskers are considered outliers and are marked with red crosses. The time
 995 resolution of CS was 8 min.

996



997

998 **Figure 8:** (a) Median and percentiles of condensation sink (CS, s^{-1}) during our observations

999 at both stations. The ‘NPF1’ and ‘non-event1’ referred to NPF and non-event days during

1000 summer 2018 and 2019, while ‘NPF2’ and ‘non-event2’ referred to NPF and non-event days

1001 during the short-term parallel observation from June 14 to July 14, 2019 at both sites. The red

1002 line represents the median of the data and the lower and upper edges of the box represent 25th

1003 and 75th percentiles of the data, respectively. The length of the whiskers represents $1.5\times$

1004 interquartile range which includes 99.3% of the data. The time resolution of CS was 8 min. (b)

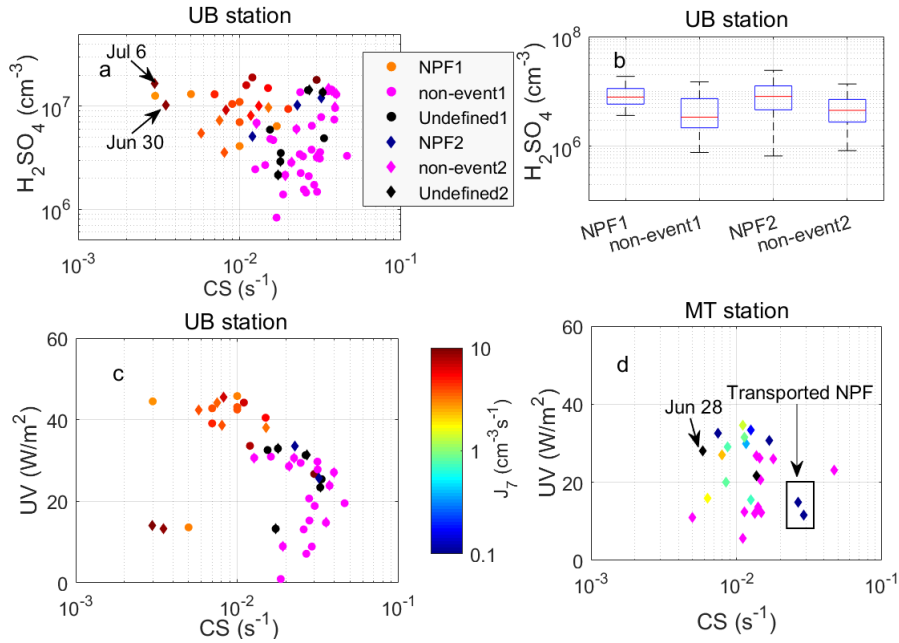
1005 Median CS during the first 2 hours of NPF events on common NPF event days measured at

1006 both stations (MT vs. UB) . (c) Numbers of NPF event, non-event and undefined days as well

1007 as NPF event frequency as a function of CS during our observation in summer 2018 and 2019

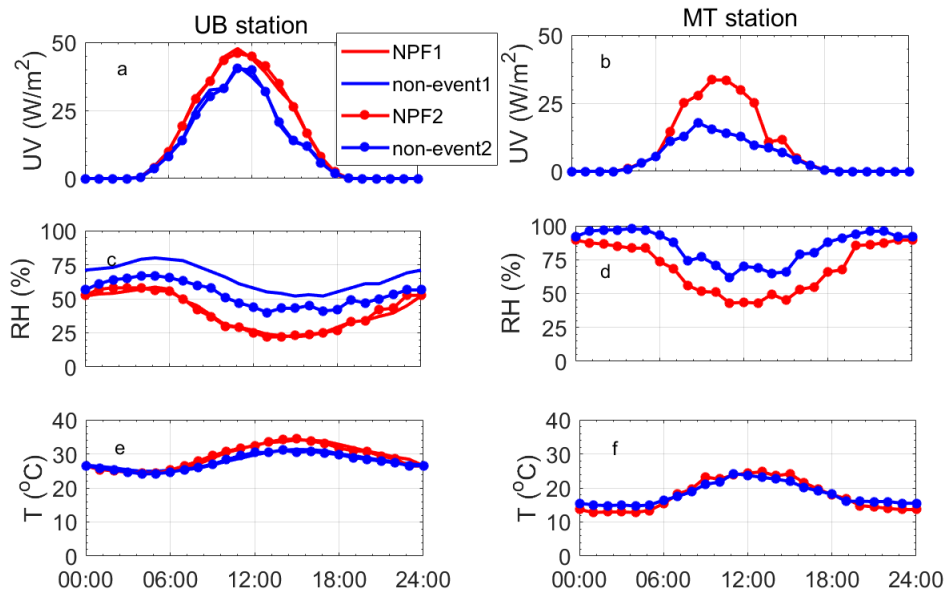
1008 at UB station.

1009



1010
 1011 **Figure 9:** (a) Median condensation sinks (CS , s^{-1}) and H_2SO_4 concentration (SA , cm^{-3}) and (b)
 1012 (b) medians and percentiles of H_2SO_4 concentration observed at UB station during the first 2
 1013 hours of NPF events and 9:00-11:00 on non-event days. (c) solar radiation ($UVA+UVB$,
 1014 W/m^2) during the first 2 hours of every NPF event and 9:00-11:00 on every non-event day at
 1015 UB station. The ‘NPF1’ and ‘non-event1’ referred to NPF event and non-event days in
 1016 summer 2018 and 2019 and the ‘NPF2’ and ‘non-event2’ referred to NPF event and
 1017 non-event days during the observation from June 14 to July 14, 2019. (d) Median
 1018 condensation sinks (CS , s^{-1}) and solar radiation ($UVA+UVB$, W/m^2) during the first 2 hours
 1019 of every NPF event and 9:00-11:00 on every non-event day at MT station. Transported NPF
 1020 event cases and one non-event day with air masses belonging to west group (Jun 28) were all
 1021 pointed out in the figure. Size of data points on NPF event days means particle formation rate
 1022 (J_7 , $cm^{-3}s^{-1}$) when it can be calculated reliably. The time resolution of CS was 8 min at UB
 1023 station and 4 min at MT station, respectively. The time resolution was 30 min for SA data at
 1024 UB station and 1h for solar radiation data at both stations.

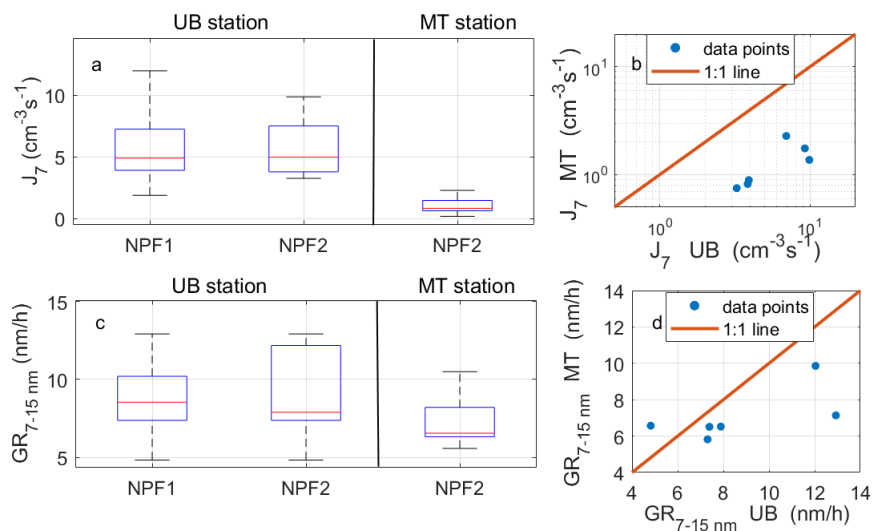
1025
 1026



1027

1028 **Figure 10:** (a, b) Diurnal pattern of solar radiation (UV, W/m²), (c, d) Temperature (T, °C),
 1029 and (e, f) Relative humidity (RH, %), at UB (left panel) and MT (right panel) stations on both
 1030 NPF event and non-event days. Time resolutions for all data points here were 1h. The ‘NPF1’
 1031 and ‘non-event1’ referred to NPF event and non-event days in summer 2018 and 2019 and
 1032 the ‘NPF2’ and ‘non-event2’ referred to NPF event and non-event days during the
 1033 observation from June 14 to July 14, 2019.

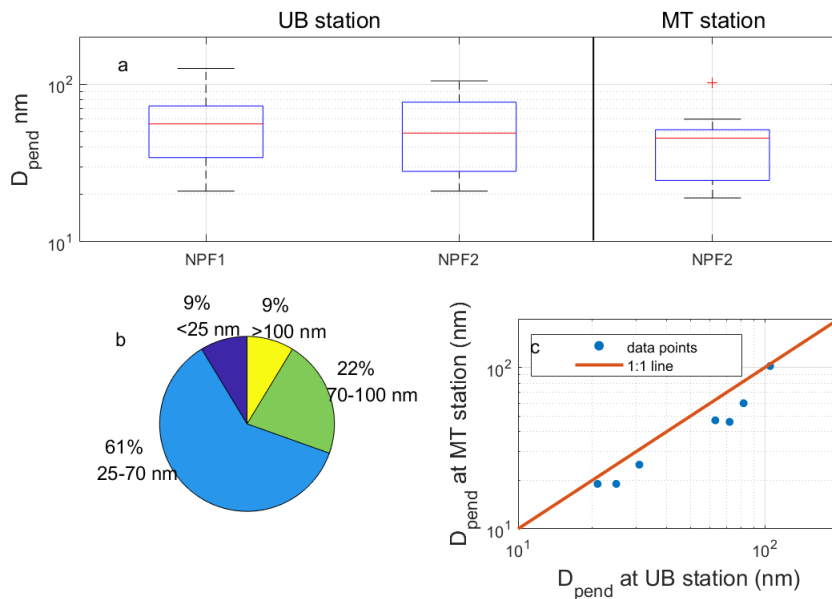
1034



1035

1036 **Figure 11:** Median and percentages of particle formation rates of 7 nm (J_7 , $\text{cm}^{-3}\text{s}^{-1}$) (a) and
 1037 particle growth rates from 7 to 15 nm ($\text{GR}_{6-15 \text{ nm}}$, nm/h) (c) measured at both stations during
 1038 our observation as well as comparison between J_7 (b) and $\text{GR}_{6-15 \text{ nm}}$ (d) of common NPF
 1039 events. The red line represents the median of the data and the lower and upper edges of the
 1040 box represent 25th and 75th percentiles of the data, respectively. The length of the whiskers
 1041 represents 1.5 \times interquartile range which includes 99.3% of the data. The ‘NPF1’ and
 1042 ‘non-event1’ referred to NPF event and non-event days in summer 2018 and 2019 and the
 1043 ‘NPF2’ and ‘non-event2’ referred to NPF event and non-event days during the observation
 1044 from June 14 to July 14, 2019.

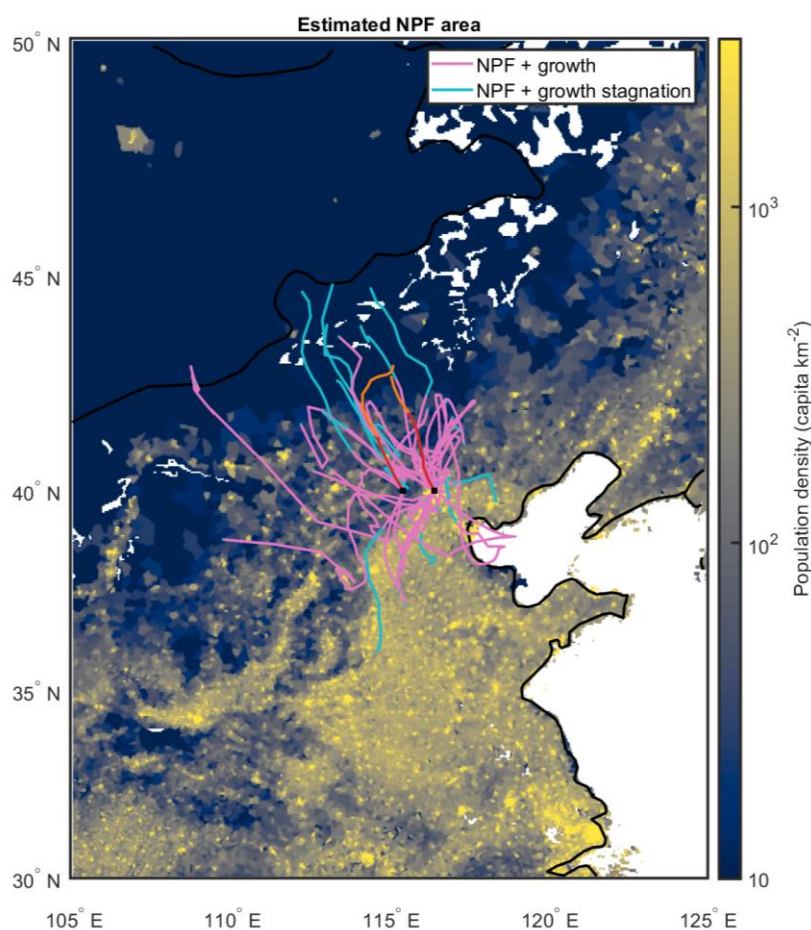
1045



1046

1047 Figure 12: (a) Median and percentiles of end diameters (D_{pend} , nm) of NPF events measured
 1048 at both sites. The red line represents the median of the data and the lower and upper edges of
 1049 the box represent 25th and 75th percentiles of the data, respectively. The length of the whiskers
 1050 represents $1.5 \times$ interquartile range which includes 99.3% of the data. The ‘NPF1’ and
 1051 ‘non-event1’ referred to NPF event and non-event days in summer 2018 and 2019 and the
 1052 ‘NPF2’ and ‘non-event2’ referred to NPF event and non-event days during the observation
 1053 from June 14 to July 14, 2019. (b) Frequencies of end diameters in the size range of smaller
 1054 than 25 nm, 25-70 nm, 70-100 nm and above 100 nm during our observation at UB station in
 1055 summer 2018 and 2019. (c) Comparison between end diameters of common NPF events at
 1056 both stations.

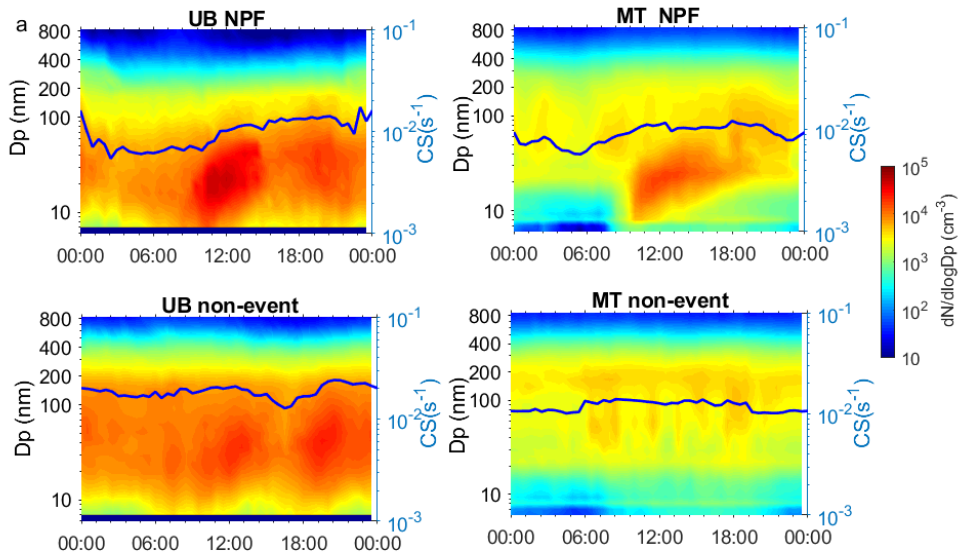
1057



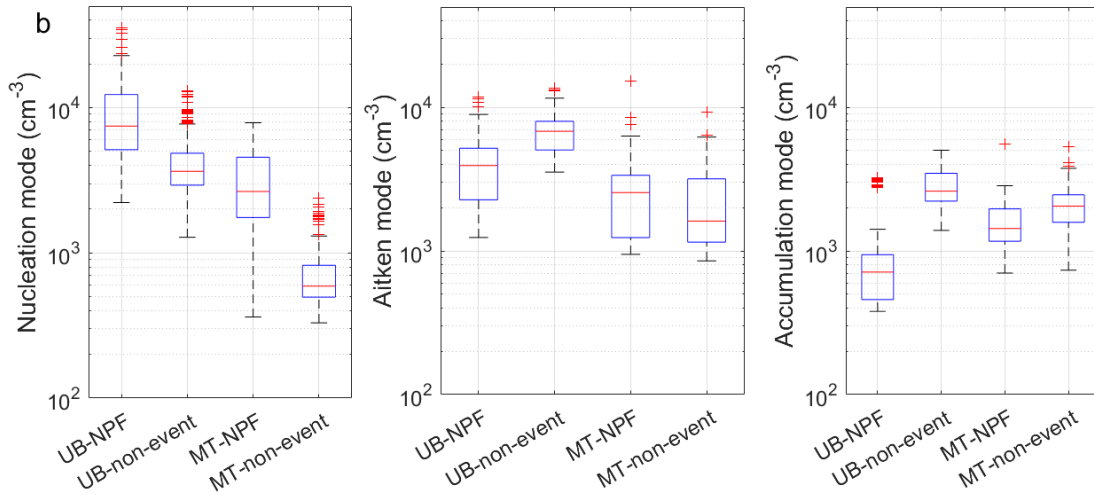
1058

1059 **Figure 13:** Spatial extent of the area where new particle formation events are estimated to
 1060 have taken place based on air mass back trajectories and the observed NPF events at both
 1061 sites. Each line represents a single NPF event and extends to the point beyond which
 1062 continuation of the mode formed in an NPF event was no longer observed at the
 1063 measurement site. In other words, if an air mass is located outside the area roughly outlined
 1064 by the colored lines during the typical onset time of NPF and then transported to our
 1065 measurement sites, NPF is unlikely to have occurred in said air mass. The lines change color
 1066 from pink to light blue if the observed NPF event enters a stage of growth stagnation, which
 1067 can indicate a less favorable environment for the formation and growth of new particles. The
 1068 lines for the case study day of June 30, 2019 are marked with red and change color to orange
 1069 if growth stagnation occurs. The lines are overlaid on top of a population density map
 1070 (Gridded Population of the World; GPWv4.10; CC BY 4.0), which is used to illustrate the
 1071 level of anthropogenic activities and emissions.

1072



1073

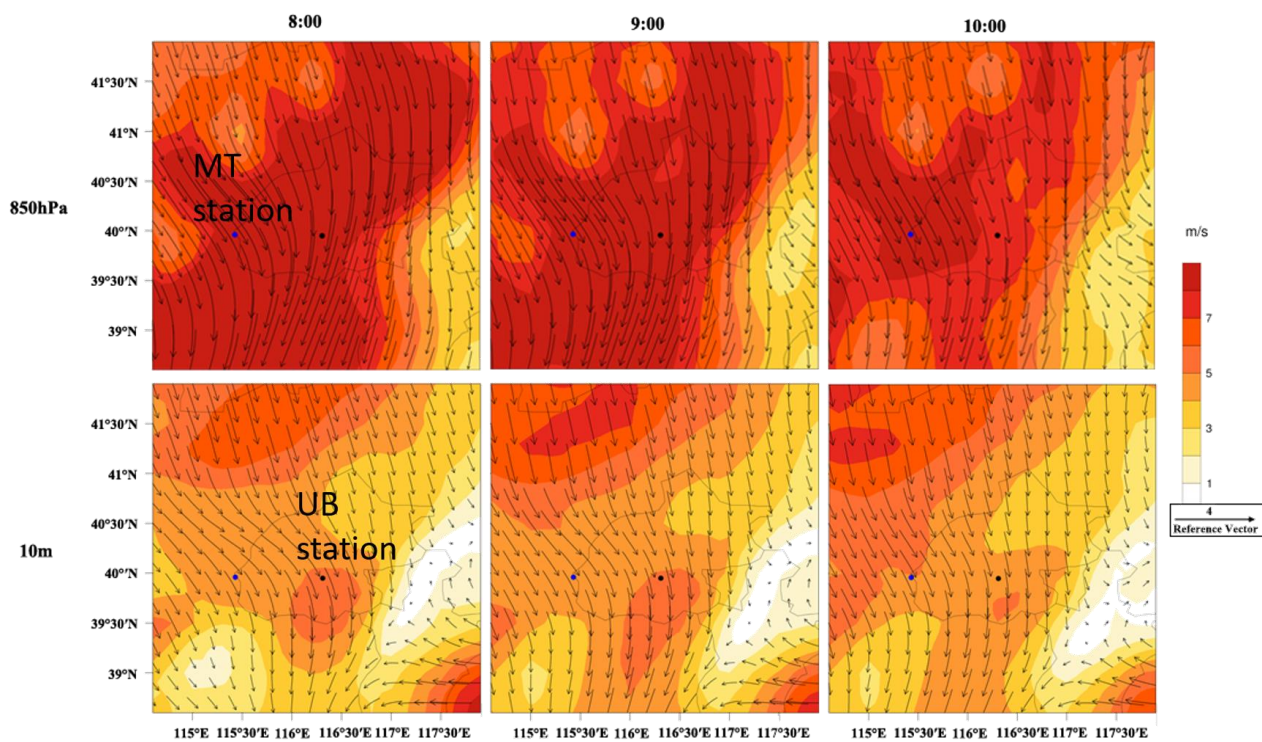


1074

1075 **Figure 14:** (a) Median particle number size distribution as well as CS (blue lines) on NPF
 1076 event and non-event days at UB (left panel) and MT (right panel) stations and (b) median and
 1077 percentiles of nucleation, Aitken and accumulation modes particle number concentration on
 1078 NPF event and non-event days during our observation from June 14 to July 14, 2019 at both
 1079 stations. The red line represents the median of the data and the lower and upper edges of the
 1080 box represent 25th and 75th percentiles of the data, respectively. The length of the whiskers
 1081 represents 1.5× interquartile range which includes 99.3% of the data. Data outside the
 1082 whiskers are considered outliers and are marked with red crosses.

1083

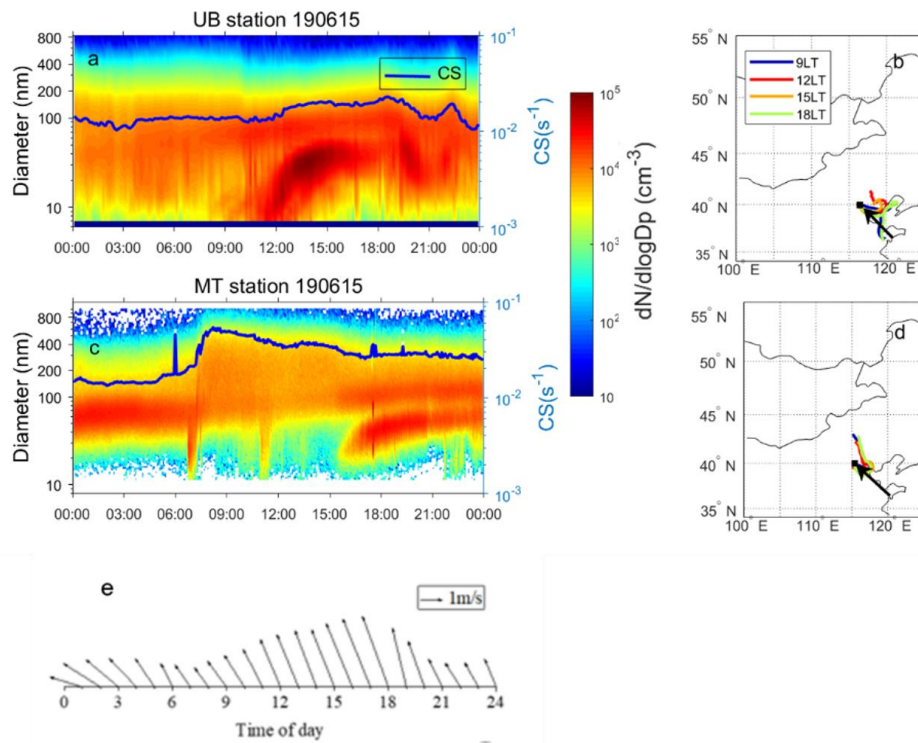
1084



1085

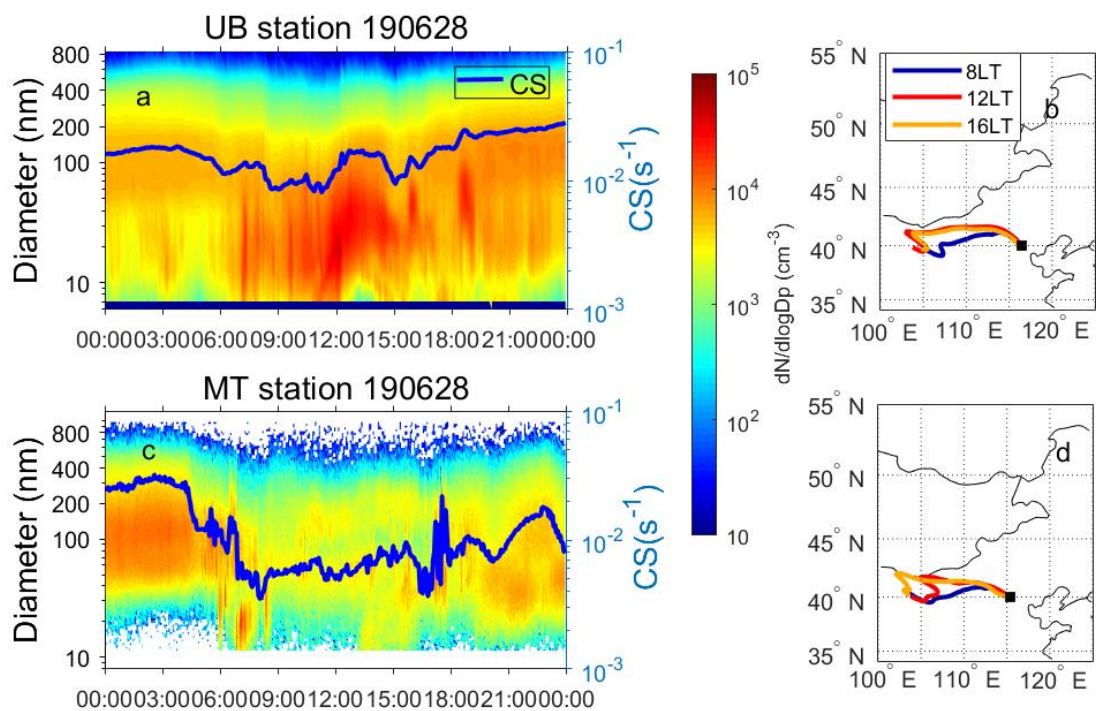
1086 Figure 15: Wind distribution at 8:00, 9:00 and 10:00 on June 30, 2019 at 10 m above the
1087 ground level (lower panel) and 850 hPa (close to the altitude of MT station, upper panel). The
1088 blue and black points on the figures represent MT and UB stations, respectively.

1089



1090

1091 **Figure 16:** Time series of particle number size distribution, CS (blue lines) and air masses
 1092 arrived at UB (upper panel) and MT (bottom panel) stations as well as wind conditions at MT
 1093 station on June 15, 2019. Time resolution for particle number size distribution data and CS
 1094 were both 8 min at UB station and 4 min at MT station, respectively. Time resolution for
 1095 wind condition data was 1h at MT station. The arrows in the figure denotes directions of
 1096 prevailing air masses before arriving at both stations during 9:00-15:00 LT.

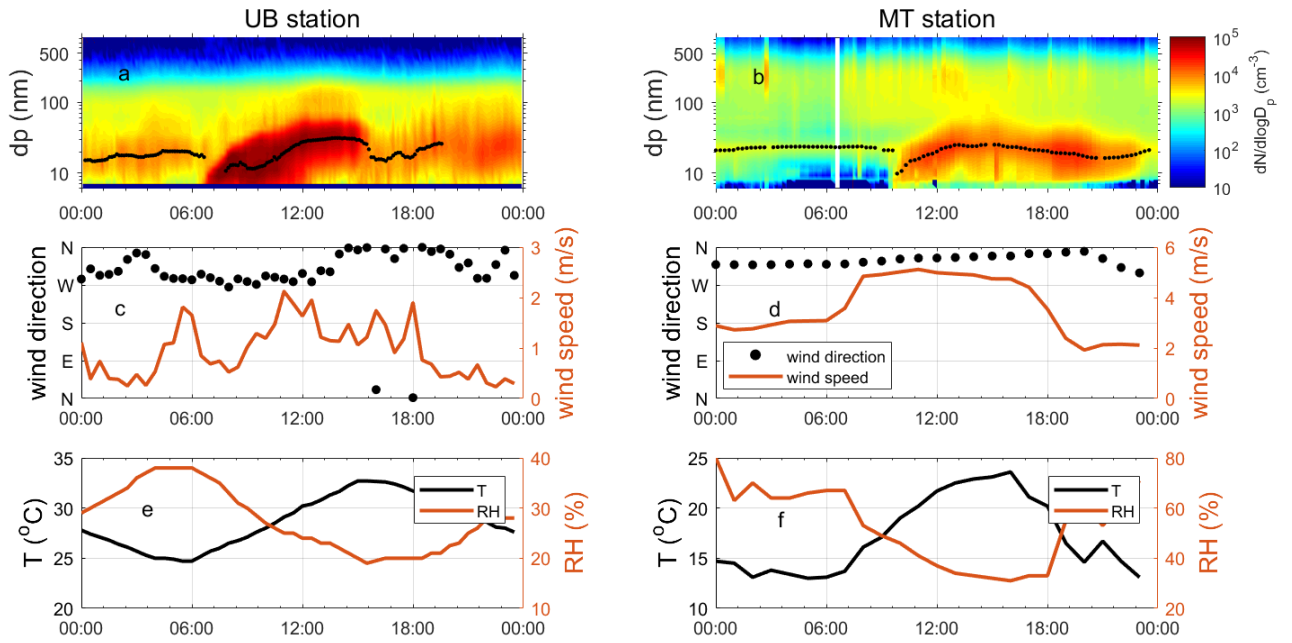


1097

1098 **Figure 17:** Time series of particle number size distribution, CS and air masses arrived at UB
 1099 (upper panel) and MT (bottom panel) stations on June 28, 2019. Time resolution for particle
 1100 number size distribution data and CS were both 8 min at UB station and 4 min at MT station,
 1101 respectively.

1102

1103



1104

1105 Figure 18: Time series of particle number size distribution and mode diameters (a, b), wind
1106 speed and direction (c, d), temperature and RH (e, f) measured at UB (left panel) and MT
1107 (right panel) on June 30, 2019.